

Experimental Investigation and Fundamental Understanding of a Full-Scale Slowed Rotor at High Advance Ratios



Anubhav Datta*
Science and Technology Corporation
U. S. Army Aeroflightdynamics Directorate



Hyeonsoo Yeo
Aeroflightdynamics Directorate (AMRDEC)
U. S. Army Research Development and Engineering Command



Thomas R. Norman
Aeromechanics Branch
NASA

Ames Research Center, Moffett Field, CA

This paper describes and analyzes the measurements from a full-scale, slowed revolutions per minute (rpm), UH-60A rotor tested at the National Full-Scale Aerodynamics Complex 40- by 80-ft wind tunnel up to an advance ratio of 1.0. A comprehensive set of measurements that includes performance, blade loads, hub loads, and pressures/airloads makes this data set unique. The measurements reveal new and rich aeromechanical phenomena that are unique to this exotic regime. These include reverse chord dynamic stall, retreating side impulse in torsion load, large inboard-outboard elastic twist differential, diminishing rotor forces and yet a dramatic buildup of blade loads, and high blade loads and yet benign levels of vibratory hub loads. The objective of this research is the fundamental understanding of these unique aeromechanical phenomena. The intent is to provide useful knowledge for the design of high-speed, high-efficiency, slowed rpm rotors of the future and a database for validation of advanced analyses.

Nomenclature

A_T	effective tunnel cross-sectional area
$C_{D,A,H}$	rotor drag $\div \rho\pi R^2(\Omega R)^2$
$C_{L,N,T}$	rotor thrust $\div \rho\pi R^2(\Omega R)^2$
C_{DE}	effective drag coefficient = $(C_{Pi} + C_{Po})/\mu = C_P/\mu - C_X$
C_P	power coefficient = $P/\rho\pi R^2(\Omega R)^3 = C_Q$
C_{Pi}	induced power coefficient
C_{Po}	profile power coefficient = $C_{Qo} + \mu C_{Ho}$
C_Q	torque coefficient = $Q/\rho\pi R^2(\Omega R)^2 R = C_P$
C_{Qi}, C_{Qo}	induced and profile torque coefficient
C_p	pressure coefficient = $2(p - p_\infty)/\rho U^2$
C_p^*	sonic pressure coefficient
C_X	propulsive force coefficient = $-C_D$
D, A, H	rotor drag in wind, horizontal, and shaft axes, lb
L, N, T	rotor thrust in wind, vertical, and shaft axes, lb
L/D_E	lift-to-drag ratio = C_L/C_{DE}
M, M_l	sectional and surface Mach number
M_A	advancing tip Mach number

M_T	tip Mach number = $\Omega R/a$
$M^2 c_c$	chord force per unit span $\div \frac{1}{2}\rho a^2 c$
$M^2 c_m$	1/4-c pitch. mom. per unit span $\div \frac{1}{2}\rho a^2 c^2$
$M^2 c_n$	normal force per unit span $\div \frac{1}{2}\rho a^2 c^2$
P, Q	rotor power, torque; $P = \Omega Q$
R	rotor radius
U	sectional speed = $\Omega r + V \sin \psi$
V	tunnel speed
X	propulsive force = $-D$
a	speed of sound
c	local chord
c_l, c_d	sectional lift and drag coefficients
p, p_∞	surface and free-stream pressures
q	tunnel dynamic pressure, $(1/2)\rho V^2$
r	radial location
α_s, α	geometric and net shaft angles, $\alpha = \alpha_s + \Delta\alpha$ (+ve back)
γ	heat capacity
$\Delta\alpha$	tunnel correction angle, +ve in up wash
δ_w	Prandtl-Glauert boundary correction factor
θ_{75}	collective angle at 75% R , deg
θ_{1S}, θ_{1C}	longitudinal and lateral cyclics, deg
λ, λ_i	inflow and induced inflow, $\lambda = \lambda_i - \mu \sin \alpha$
μ	advance ratio, $V/\Omega R$
ρ	free-stream density
σ	rotor geometric solidity
ψ	azimuthal location, deg; 0° when blade is above tail line
Ω	rotor rotational speed

*Corresponding author; email: hubloads@gmail.com.

Concise version of paper presented at the American Helicopter Society 67th Annual Forum, Virginia Beach, VA, May 27-29, 2011. This paper received the Best Paper in Dynamics and Alfred P. Gessow awards. Manuscript received August 2011; accepted January 2013.

Introduction

Slowed rotors are recognized as technology enablers for higher speeds in edgewise rotors and higher cruise efficiencies in tiltrotors. Even at low speeds, optimal use of rotor speed can offer significant efficiency gains, assuming a required thrust level can be maintained. As a result, considerable attention is devoted today toward the development of wide speed range power turbines and continuously variable multiple-speed transmissions for rotorcraft (Refs. 1, 2). Some of these technologies are already available today in limited form and have found application on advanced rotorcraft. For instance, a 15%–20% reduction in engine speed is deliverable by today's commercial power turbines with no more than 5%–10% penalty in specific fuel consumption (Ref. 3). The Sikorsky X2 Technology Demonstrator can slow its rotor by 20% from 446 to 360 revolutions per minute (rpm) using this technology (Refs. 4, 5). The Bell/Boeing V-22 Osprey slows its rotor by 19% from 412 to 333 rpm to fly in cruise. Two-speed transmissions, with innovative gearboxes and clutches for changing gears in flight, have also been demonstrated. Frontier Systems' optimum speed rotor—now part of Boeing's 6500-lb A160 unmanned air vehicle (UAV)—uses a similar technology on edgewise rotors for high-efficiency low-speed flight (Ref. 6). It is now being pursued on tiltrotors for high-efficiency high-speed flight (Ref. 7). Even though the underlying technology of rpm reduction remains the same in both edgewise rotors and tiltrotors, the aeromechanics of their operations is entirely different. An edgewise rotor, when slowed down for the purposes of high speed, begins to operate at very high, nonconventional advance ratios ($\mu = 0.7$ –1.0 and beyond). A large part of its retreating side now remains immersed in reverse flow. The objective of this research is to understand the aeromechanics of such a regime.

High advance ratios are traditionally associated with autogiros (Ref. 8) or helicopter-autogiro hybrids (Refs. 9, 10). For a helicopter to achieve high speeds (200–300 kt) and yet remain efficient and maneuverable, the rotor must remain powered and controlled, while reducing rpm to maintain a low advancing tip Mach number. The word slowed rotor refers to such rotors. By definition, slowed rotors generate lower forces and moments and are therefore intended primarily for use in compound helicopters (with the exception of lightweight UAVs). The decades of the 1960s and 1970s saw extensive research, development, and flight-testing of a wide variety of compound helicopters (Ref. 11). The developments spurred significant research on high advance ratio slowed rotors, yet none actually found a place on an aircraft at the time. The U.S. Army XH-51A (Lockheed) experimented with rpm reduction but only down to 95% nominal, below which structural resonance problems were encountered (Ref. 12). Ultimately, none of these aircraft entered regular production. Today, with advances in materials, controls, and engine/drivetrain technologies, compounds have once again emerged as potential contenders for high-speed heavy-lift rotorcraft (Ref. 13)—this time, envisioned to be equipped with slowed rotors. A vision for the future is a 50% or more reduction in rpm.

Extensive analytical investigations of slowed rotors were performed in the past decade (Refs. 14–18). Successful flight demonstrations of three modern compounds were also carried out, namely the Sikorsky X2 with a coaxial rotor and pusher prop (Ref. 19), the Eurocopter X³ with a wing and two wing-mounted propellers (Refs. 20, 21), and the Piasecki X-49A with a wing and a vectored thrust ducted propeller (Ref. 22). The coaxial X2 flew at advance ratio of $\mu = 0.8$ at 80%–85% nominal rpm (hover) to demonstrate successful flight at 250 kt. The single rotor X³ demonstrated 180 kt with the eventual goal of reaching 220 kt at advance ratio of $\mu = 0.66$ at 78% nominal rpm. Additionally, CarterCopter's successful demonstration of the first ever $\mu = 1.0$ flight in 2005 with 50% reduced rpm, even though as an autogiro, also contributed to growing interest in high advance ratio slowed rotors (Ref. 23).

A slowed rotor must operate as a conventional rotor in hover and yet all but disappear—in terms of drag, loads, and vibration—at high speeds. Understanding the fundamental dynamics of rotors in these conditions is important to meet this technical challenge efficiently (minimizing vehicle power) and safely (avoiding control reversal and excessive loads and vibration). Unlike conventional rotors, there is a scarcity of experimental data and a lack in the fundamental understanding of the aerodynamic and dynamic environment of high-advance-ratio slowed rotors. Historically, only four full-scale high-advance-ratio tests are documented: the four-bladed, 22.5-ft radius, articulated Pitcairn PCA-2 autogiro tested in the NACA Langley 30- by 60-ft wind tunnel (Ref. 24); a two-bladed, 7.625-ft radius, teetering rotor tested in the same tunnel (Refs. 25, 26); a four-bladed, 28-ft radius, articulated rotor and a two-bladed, 17-ft radius, teetering rotor tested in the NASA Ames 40- by 80-ft wind tunnel (Ref. 27); and the same two-bladed, 17-ft radius, teetering rotor tested again but with reduced built-in twist in the same tunnel (Ref. 28). All of these tests, conducted during the 1960s (the autogiro test was in 1930s), provide only rotor performance and blade root motions and limited flow visualization (tufts). Recently, a comprehensive study conducted on correlating these data with analyses (Ref. 29) highlighted the discrepancies in current analyses—both lifting-line and computational fluid dynamics based—in predicting high-advance-ratio performance. These discrepancies cannot be addressed systematically in the absence of detailed test data.

There have been several model-scale tests beginning with the seminal work of Meyer and Falabella on three-bladed, 2.5-ft radius, articulated, and hingeless rotors at the MIT 7- by 10-ft tunnel (Ref. 30), a four-bladed, 4.5-ft radius, articulated rotor at the UTRC 18-ft octagonal tunnel (Ref. 31), a four-bladed, 4-ft radius articulated rotor at the NASA Ames 12-ft pressure tunnel (up to $\mu = 2.46$, the highest thus far) (Ref. 32), to the recent three-bladed, 2.16-ft radius, flap-articulated autogiro tested at the University of Maryland (UMD) 7.5- by 11-ft tunnel (Ref. 33). All of these tests have focused on performance with very limited loads data, and none with airloads, except for Meyer and Falabella. Meyer and Falabella measured airloads but the rotor was not trimmed (no cyclics), and hence the airloads were not representative of true flight. Berry and Chopra (Ref. 34) carried out model-scale tests on a four-bladed, 3-ft radius, articulated rotor at the UMD tunnel recently to address some of the above technical deficiencies—though not the lack of airloads.

In an effort to address the lack of comprehensive data and fundamental understanding, a full-scale UH-60A rotor (4-bladed, 26.83-ft radius, fully articulated) was tested at the U.S. Air Force's National Full-Scale Aerodynamics Complex (NFAC) 40- by 80-ft wind tunnel at slowed rpm—65% and 40% of nominal—and high speeds with advance ratios reaching up to 1.0. A comprehensive set of measurements including performance, blade loads, hub loads, and pressures/airloads make this data set unique. The test was part of a broader program (Ref. 35) that was divided into six phases. The first five phases involved conventional operations: 1-g level flight speed sweeps, parametric sweeps, reproduction of earlier flight test and Duits–Nederlandse wind tunnel test points, and particle image velocimetry conditions. The sixth phase was the high-advance-ratio slowed rotor test—the subject of this paper. The objective was to explore the aeromechanics of a conventional (edgewise) rotor in a nonconventional (large reverse flow) regime in anticipation of the next generation of high-speed, high-efficiency, variable rpm rotors.

Scope of paper

The present test differs from those conducted earlier in that it acquires a complete set of measurements (performance, motions, structural loads, hub loads, and pressures/airloads) under slowed rpm, high-advance-ratio

conditions. This is also the first test of a real (production) rotor at high advance ratios. The emphasis of this paper is on the fundamental understanding of aeromechanics in the high-advance-ratio regime, by relating flow phenomena to rotor performance and to structural loads. The first section provides a brief description of the experiment, emphasizing the special considerations of the slowed rotor test. The second section describes the test points. The following three sections examine specific results from this test: performance, structural loads and hub loads, and pressure and airloads. Throughout the paper, the words thrust level mean either blade loading C_T/σ or dimensional thrust depending on context. The advance ratio is used to mean tip speed ratio.

Some of the data are revised from those originally published in Ref. 36. Most importantly, the revised pressure plots now show lesser transonic flow. The other minor revisions are in cyclic control angles (the change in lateral cyclic is significant), structural loads at 20% and 40% R , and the inclusion of two additional transducer data at 22.5% R (these were originally deemed unreliable) in the pressure plots.

Description of Experiment

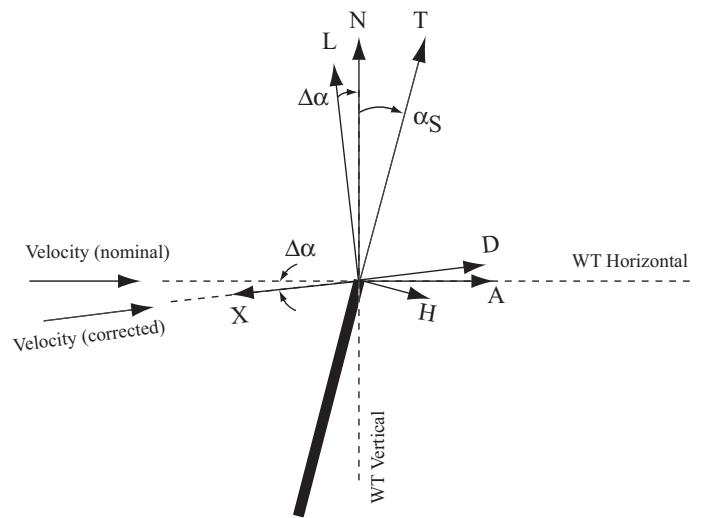
The details of the hardware, data reduction, and pretest activities common to all six test phases are described in Ref. 35. A brief summary is provided here, with particulars relevant to this test.

Model: The UH-60A rotor mounted on the NFAC Large Rotor Test Apparatus (LRTA) is shown in Fig. 1(a). A schematic of the model defining the force conventions is given in Fig. 1(b). The Prandtl–Glauert wall correction is $\Delta\alpha = \delta_w N/(qA_T)$ radians. Based on the rotor diameter to tunnel width ratio and model offset from centerline (10.9 inches up), the correction factor is $\delta_w = 0.0915$. Using δ_w and the disk and tunnel areas: $\Delta\alpha = 8.61(C_N/\mu^2)$ deg.

Instrumentation: The blades are the same four blades flown during the 1993 Airloads Program (Ref. 37), but refurbished and recalibrated with new instrumentation. A total of 332 rotor and hub measurements and a total of 124 LRTA and wind tunnel measurements were acquired. The rotor and hub measurements included: 160 working pressure transducers (down from 215 functional transducers at the beginning of test, out of 235) arranged over nine spanwise stations (22.5, 40, 55, 67.5, 77.5, 86.5, 92, 96.5, and 98.9% R), across 10–15 chordwise stations (depending on span station), and a few intermediate stations; 26 two- or four-leg strain-gauge bridges on a second instrumented blade for structural loads at the root (11.3% R) and eight uniformly distributed spanwise stations from 20% to 90% R ; two independent blade motion hardware—a set of three rotary variable differential transformers mounted on each blade hinge point and a set of three laser distance transducers mounted on each blade hub arm; eight strain gauge bridges on the shaft—four to measure shaft stresses and four to measure shaft bending moments; and 10 four-leg strain-gauge bridges to measure axial loads—four on the pitch links, four on the damper, and two on the rotating scissors. The LRTA and wind tunnel measurements included: a five-component rotor balance—four flexures instrumented with 12 primary and 12 backup gauges for three hub forces and hub pitching and rolling moments, and an in-line flex coupling for torque; eight strain-gauge bridges to measure nonrotating control system forces and moments—three bridges on stationary pushrods, one bridge on stationary scissor, and four on the swashplate guide; six displacement measurements—three each for the primary and dynamic actuators; six load cells between LRTA fairing and chassis for steady fuselage loads; 31 tunnel pressure/temperature measurements; three model angle measurements; and a rotor rpm measurement. The blade pressure data were acquired at 2048 samples per revolution (/rev). The motions and loads data were acquired at 256 samples/rev.



(a) Full-scale UH-60A rotor installation



(b) Schematic showing axes definitions

Fig. 1. Full-scale UH-60A rotor installed on the LRTA in the NFAC 40- by 80-ft wind tunnel; model shaft angle α_S , wall correction $\Delta\alpha$, and rotor forces in tunnel axes (N and A), shaft axes (T and H), and corrected wind axes (L and D), and the propulsive force ($X = -D$).

Motion and loads allowables: Several special steps were taken for the slowed rotor test including those based on Sikorsky's review of the motions and loads allowables at reduced rpm. The main rotor dynamic flap and droop stop mechanisms were modified to allow adequate flapping at the reduced rpm. The lag displacement was monitored for instabilities in case 1–3/rev motions significantly decreased damping at the lag frequency. Trailing edge strains (vibratory and positive/negative peaks) at 50% R and 68% R were added as safety of flight parameters in case decreased centrifugal forcing led to compression from edgewise bending. The lug stress at the blade cuff was confirmed not to be a concern.

Test plan and procedure: The test plan was constructed as a parametric sweep with tip Mach number M_T as the primary variable. The M_T settings were 0.65 at 100% nominal rpm (NR) of 258, 0.42 at 65% NR and 0.26 at 40% NR. The maximum forward speed was limited to 182 kt (maximum tunnel speed is 300 kt). The minimum rpm (40% NR) and the maximum forward speed were set by safety of flight considerations. These limits

determined the maximum advance ratio. All rpm changes were carried out after reducing the tunnel speed to zero or to a very low value (nominal hover), to avoid resonance during changing blade frequencies. Similarly, all shaft angle changes were carried out at zero or low tunnel speeds, to avoid large transient blade flapping. The emergency shutdown procedure was to reduce the tunnel speed first. The test procedure was (1) set M_T ; (2) set shaft angle α_S ; (3) vary tunnel speed for intended μ ; (4) at each μ , acquire data over a range of collective angles with the maximum limited by cyclic control limits or load limits whichever was encountered first (usually the latter); and (5) after completion of the collective sweeps at all μ , reduce tunnel speed and change α_S . Each collective setting was a test point. At each test point, the rotor was manually trimmed to minimize 1/rev root flapping angle using 1/rev cyclic controls.

The estimated uncertainties in thrust and drag are 60 and 20 lb, respectively. The performance data will include all repeat points so that any scatter is clearly visible. The loads data are averaged over all 128 revolutions. Variations from revolution to revolution are nominally around 5% of mean for blade loads and 10% of mean for airloads with greater variations under stall. The trim targets are met nominally within errors of $-0.029^\circ \pm 0.225^\circ$ and $-0.034^\circ \pm 0.153^\circ$ for longitudinal and lateral flapping, respectively. The blade-to-blade differences are the smallest for the pitch link loads, moderate for damper loads, and the largest for the root pitch angles. More details—using the 100% NR case as example—can be found in Ref. 35.

Performance Measures

The following definitions are used for interpretation of performance. Rotor power C_P equals rotor torque C_Q in coefficient form. Torque includes induced (c_l contribution) and profile (c_d contribution) components: $C_P = C_Q = C_{Qi} + C_{Qo}$. Adding and subtracting $\mu \cos \alpha C_H = \mu \cos \alpha (C_{Hi} + C_{Ho})$, recognizing $C_{Qi} + \mu \cos \alpha C_{Hi} = \int \lambda dC_T$, and defining profile power as $C_{Po} = C_{Qo} + \mu \cos \alpha C_{Ho}$ leads to $C_P = \int \lambda dC_T + C_{Po} - \mu \cos \alpha C_H$ (note that $\mu = V/\Omega R$ here, not $V \cos \alpha / \Omega R$). Separating inflow into induced and forward speed components as $\lambda = \lambda_i - \mu \sin \alpha$, recognizing $C_T \sin \alpha + C_H \cos \alpha = C_D - C_X$ (see Fig. 1(b)), and defining induced power as $C_{Pi} = \int \lambda_i dC_T$, leads to the energy balance expression

$$C_P = C_{Pi} + C_{Po} + \mu C_X \quad (1)$$

The μC_X term is power for propulsion. The remainder is associated with the wing-like action of the rotor and represented as an effective drag C_{DE} , where $\mu C_{DE} = C_{Pi} + C_{Po}$. Thus effective drag is $C_{DE} = C_P/\mu - C_X$. Rotor efficiency (lift to drag ratio) follows

$$L/D_E = \frac{C_L}{C_P/\mu - C_X} \quad (2)$$

Slowed Rotor Test Matrix

The slowed rotor test points are summarized in Table 1. There are a total of 232 points; 47 of these are 100% NR points carried out at three shaft angles of 0° , 2° , and 4° ; 36 are 65% NR points at a single shaft angle of 0° ; and 149 are 40% NR points at three shaft angles 0° , 2° , and 4° . The 40% NR points constitute the most comprehensive set. The maximum advance ratio of $\mu = 1.0$ was achieved during this set.

The matrix of the test points (Fig. 2) indicates a useful separation of compressibility and reverse flow regimes. The largest variation of μ (i.e., extent of reverse flow) from 0.3 to 1.0 is contained entirely within the subsonic regime. There are two sets of points that have common speeds at different rpm. The speed 139 kt is a common speed between 65% and 40% NR (with $\mu = 0.5$ and 0.8, respectively). Similarly, the

Table 1. Slowed rotor test runs

Run no.	% NR	α_S	V	μ	M_A	θ_{75}
R66	100	0.0	130	0.3	0.85	-0.1 to 10.0
		2.0				0.0–9.9
		4.0				-0.1 to 5.9
R69		0.0	172	0.4	0.91	0.4–7.9
		2.0				-0.1 to 8.0
		4.0				0.0–5.9
R87	65	0.0	83	0.3	0.55	-0.1 to 7.9
			111	0.4	0.59	-0.1 to 7.9
			139	0.5	0.63	-0.1 to 7.9
			167	0.6	0.67	0.0–7.9
R91	40	0.0	52	0.3	0.34	0.0–8.0
			69	0.4	0.36	-0.1 to 8.0
			87	0.5	0.39	0.0–8.0
			104	0.6	0.42	0.0–7.9
			121	0.7	0.44	0.0–8.0
			139	0.8	0.47	-0.1 to 8.0
			157	0.9	0.49	0.0–4.0
			174	1.0	0.52	-0.1, 0.9, 1.9
R96		2.0	52	0.3	0.34	1.7, 1.9
			70	0.4	0.36	1.9
			87	0.5	0.39	1.9
			104	0.6	0.42	2.0
			121	0.7	0.44	1.9
			139	0.8	0.47	1.9
			156	0.9	0.49	1.9
			174	1.0	0.52	0.9
R93		4.0	52	0.3	0.34	0.0–8.0
			70	0.4	0.36	0.0–8.0
			87	0.5	0.39	-0.1 to 8.0
			104	0.6	0.42	0.0–8.0
R95			52	0.3	0.34	0.9, 1.1
			104	0.6	0.36	0.0, 2.0, 3.0
			121	0.7	0.44	-0.1 to 7.7
			138	0.8	0.47	-0.1 to 7.7
			156	0.9	0.49	-0.1 to 6.2
			173	1.0	0.52	0.0, 2.0

speed 174 kt is common between 100% and 40% NR (with $\mu = 0.4$ and 1.0, respectively). In other words, the nominal rotor at $\mu = 0.4$ flies at the same speed as the 40% NR rotor at $\mu = 1.0$. The 65% NR rotor at $\mu = 0.5$ flies at the same speed as the 40% NR rotor at $\mu = 0.8$. There is a pair of points that represents a common advancing tip Mach number but widely different advance ratios—the 65% NR, $\mu = 0.3$ point and the 40% NR, $\mu = 1.0$ point. The nondimensional thrust speed envelopes for the three rpm are shown in Fig. 3. The rotor generated drag at all points, but never operated in autorotation.

From the test matrix, test points for parametric sweeps are identified for the purposes of studying structural loads, hub loads, and airloads. The first two digits of each test point in Table 2 identify the run number. Table 2 shows two rpm sweeps at advance ratios of 0.3 and 0.4 and two advance ratio sweeps at shaft angles 0° and 4° . The rpm sweeps isolate the effects of slowing the rotor while keeping the reverse flow area the same. The advance ratio sweeps isolate the effects of increasing the reverse flow area. There is a common thrust level in the two sweeps so that they can be used to study the effect of shaft angle variation. Table 3 shows six thrust sweeps—one set each for shaft angles of 0° and 4° , and

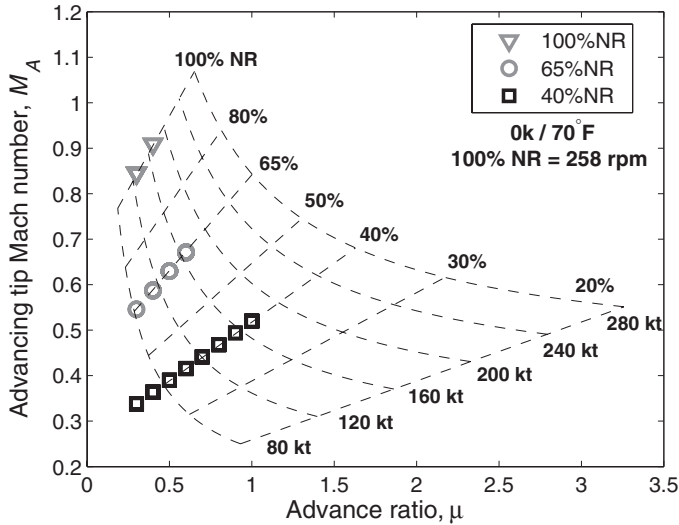


Fig. 2. Advancing tip Mach number versus advance ratio of all slowed rotor test points.

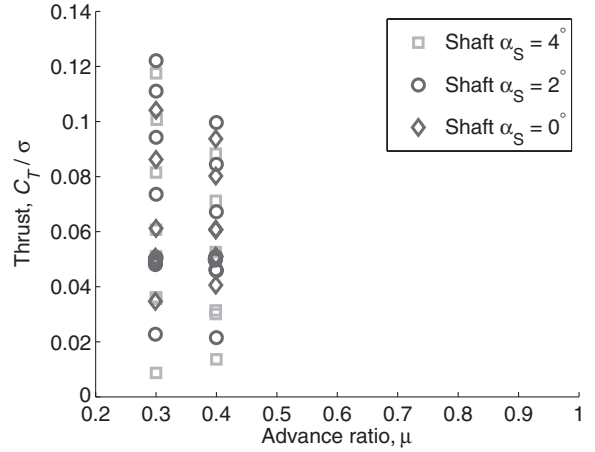
Table 2. Test points for rpm sweeps at two different advance ratios and advance ratio sweeps at 40% nominal rpm at two different shaft angles

Point	M_T	α_S	μ	θ_{75}	C_T/σ	T	θ_{1C}	θ_{1S}
rpm sweeps								
$\mu = 0.3$								
6619	0.65	0.0	0.3	6.0	0.0815	18407	0.4	-4.6
8716	0.42	0.0	0.3	5.9	0.0806	7797	1.6	-5.1
9117	0.26	0.0	0.3	5.9	0.0815	3033	2.6	-5.3
$\mu = 0.4$								
6912	0.65	0.0	0.4	6.0	0.0712	15880	-1.1	-4.8
8724	0.42	0.0	0.4	5.9	0.0699	6720	0.5	-6.3
9125	0.26	0.0	0.4	6.0	0.0722	2679	1.7	-6.5
μ sweeps								
$\alpha_S = 0^\circ$								
9116	0.26	0.0	0.3	4.0	0.0622	2307	1.5	-4.0
9133	0.26	0.0	0.5	6.0	0.0633	2338	0.9	-7.4
9145	0.26	0.0	0.6	7.9	0.0622	2277	0.3	-10.1
$\alpha_S = 4^\circ$								
9318	0.26	4.0	0.4	2.0	0.0627	2315	0.7	-4.0
9325	0.26	4.0	0.5	2.0	0.0628	2312	0.1	-4.8
9518	0.26	4.0	0.7	3.0	0.0616	2235	-0.8	-6.9
9528	0.26	4.0	0.9	6.2	0.0634	2280	-3.1	-11.6

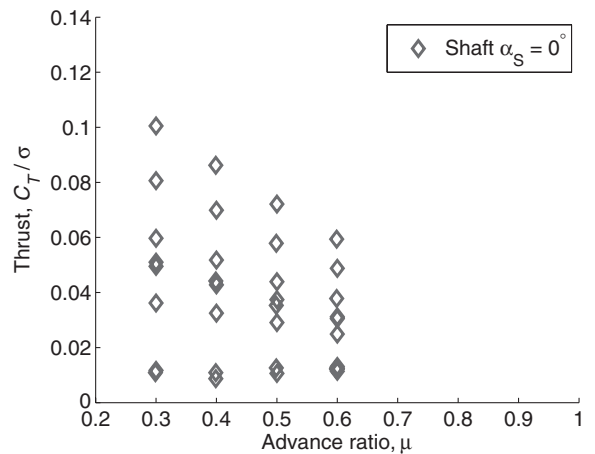
each set constituting three collective sweeps at advance ratios of 0.8, 0.9, and 1.0. The sweeps isolate the effects of reverse flow stall. Selected subsets of the above sweeps are used in this paper to illustrate the special aeromechanical phenomena of the high-advance-ratio regime.

Rotor Performance

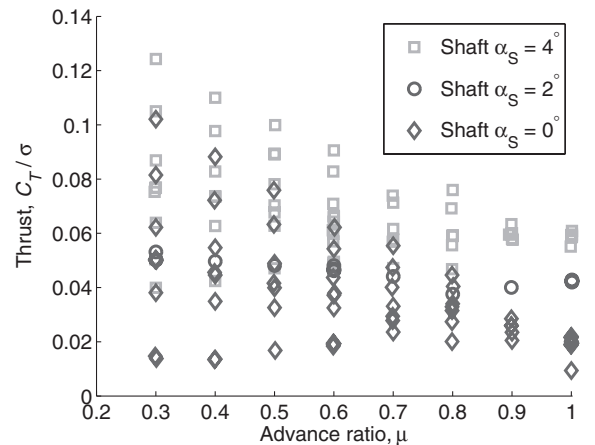
This section analyzes the measured rotor performance. The 40% NR case is studied in detail as this case extends up to $\mu = 1.0$. The 65% NR case (up to $\mu = 0.6$) and 100% NR case (up to $\mu = 0.4$) are used for comparison purposes. For all of the test points, thrust almost equals lift ($C_T \approx C_L$), but not used interchangeably to maintain consistency of nomenclature. In addition, for the case of 0° shaft angle, drag almost equals H-force ($C_D \approx C_H$).



(a) 100% NR ($\mu = 0.3$ and 0.4)



(b) 65% NR ($\mu = 0.3-0.6$)



(c) 40% NR ($\mu = 0.3-1.0$)

Fig. 3. Thrust-speed envelope at 100%, 65%, and 40% NR.

The thrust variation with collective at 0° shaft angle at 40% NR is shown in Fig. 4(a). The sensitivity is reduced to almost zero at $\mu = 1.0$. The thrust variation with collective at 4° shaft angle is shown in Fig. 4(b). The sensitivity reverses slightly at $\mu = 1.0$. The thrust sensitivities at the two shaft angles are plotted in Fig. 4(c) as a function of advance ratio. Also plotted in the same figure is the thrust sensitivity to shaft angle at

Table 3. Test points for thrust (collective) sweeps at two shaft angles and three advance ratios

Point	M_T	α_S	μ	θ_{75}	C_T/σ	T	θ_{1C}	θ_{1S}
$\alpha_S = 0^\circ$								
$\mu = 0.8$								
9155	0.26	0.0	0.8	-0.1	0.0201	727	-2.8	-0.5
9156	0.26	0.0	0.8	2.0	0.0329	1192	-2.8	-3.0
9157	0.26	0.0	0.8	4.0	0.0340	1227	-2.9	-5.9
9158	0.26	0.0	0.8	6.0	0.0404	1459	-2.9	-8.3
9159	0.26	0.0	0.8	8.0	0.0446	1618	-2.6	-10.8
$\mu = 0.9$								
9162	0.26	0.0	0.9	0.0	0.0205	736	-3.7	-0.3
9163	0.26	0.0	0.9	2.0	0.0235	844	-4.0	-3.0
9164	0.26	0.0	0.9	4.0	0.0259	930	-4.4	-6.0
$\mu = 1.0$								
9168	0.26	0.0	1.0	-0.1	0.0193	688	-4.8	0.0
9175	0.26	0.0	1.0	1.9	0.0220	784	-5.1	-2.7
$\alpha_S = 4^\circ$								
$\mu = 0.8$								
9520	0.26	4.0	0.8	-0.1	0.0468	1697	-2.1	-3.5
9521	0.26	4.0	0.8	1.9	0.0556	2014	-1.9	-5.9
9522	0.26	4.0	0.8	5.9	0.0692	2504	-1.7	-11.0
9523	0.26	4.0	0.8	7.7	0.0760	2749	-1.4	-13.0
$\mu = 0.9$								
9526	0.26	4.0	0.9	-0.1	0.0576	2064	-3.1	-3.2
9527	0.26	4.0	0.9	2.0	0.0595	2151	-3.4	-6.2
9528	0.26	4.0	0.9	6.2	0.0634	2280	-3.1	-11.6
$\mu = 1.0$								
9531	0.26	4.0	1.0	0.0	0.0609	2170	-4.0	-3.3
9530	0.26	4.0	1.0	2.0	0.0585	2085	-4.6	-6.4

0° collective. This sensitivity shows a slight increase at the lower and higher advance ratios ($\mu = 0.3 - 0.5$ and $\mu = 0.7 - 1.0$) with a dip in between but remains nominally constant compared to the sensitivity to collective.

The loss of thrust sensitivity to collective under high advance ratios (near $\mu = 1.0$) was first reported in 1965 by Jenkins (Ref. 26). An increase in collective makes the reverse flow regime more severe at high advance ratios, leads to a loss in lift on the retreating side, which then requires a drop in lift on the advancing side to trim the rotor, and consequently decreases net thrust. The drop in lift in the advancing side is brought about by a progressively higher longitudinal cyclic requirement, as seen by the increasing sensitivities of the longitudinal cyclic to collective regardless of shaft angle (Fig. 4(d)). An increase in shaft angle makes the reverse flow less severe, and because a greater reverse flow area (i.e., advance ratio) leads to a greater benefit, generally augments the effect of thrust increase with shaft angle (Fig. 4(c)). An increase in collective at a higher shaft angle (4° vs. 0°) appears to be more detrimental to thrust.

The power variation with thrust at 0° shaft angle is shown in Fig. 5(a). Each symbol represents one collective setting. Beyond $\mu = 0.7$ power reduces with increasing thrust but at the cost of increasingly greater drag as shown in Fig. 5(b). The drag sensitivity to collective increases with advance ratio, unlike thrust and shows a steep increase beyond $\mu = 0.7$. The H-force is expected to be the same as drag force at 0° shaft angle; the deviation found at the lower advance ratios and higher lift are due to the tunnel correction $\Delta\alpha$ becoming more significant. If the rotor is to be carried through air (in flight), power to the rotor must equal the rotor power measured in the tunnel plus power to overcome drag ($C_P + \mu C_D$), which simply equals induced and profile power measured in the tunnel ($C_P + \mu C_D = C_{Pi} + C_{Po}$). This is plotted in Fig. 5(c) and shows a continuous increase as expected. The effective drag (C_{DE} ,

where $\mu C_{DE} = C_{Pi} + C_{Po}$), shown in Fig. 5(d), follows the same trend, except that the lower advance ratios ($\mu = 0.3$ and 0.4) collapse to a single curve. Increasing the shaft angle makes the rotor more efficient. As shown in Fig. 6(a), the rotor consumes less induced and profile power for the same lift. The rotor efficiency (lift-to-drag ratio L/D_E) values at the two shaft angles are compared in Fig. 6(b) for high advance ratios. A positive shaft angle typically increases the efficiency of rotors; what is different for the slowed rotor is that the efficiency is maximized by a decrease in collective when operating beyond thrust reversal. This is the case for $\mu = 1.0$ at $\alpha_S = 4^\circ$ in Fig. 6(b). Further details on performance including rotor forces for zero collective sweeps (closest approximation to zero thrust sweeps that are useful for estimating profile components) can be found in Ref. 36.

In summary, the performance measurements were consistent with previous test data. A decrease in thrust sensitivity to collective at high advance ratios, along with a reversal around $\mu = 0.9 - 1.0$, was observed as expected. A steep drop in efficiency was observed at the high advance ratios. The efficiency was higher at a positive shaft angle but at the expense of greater drag.

Blade Loads and Hub Loads

In this section, the blade structural loads and hub loads are compared between the nominal and slowed rotors.

The structural loads are examined in dimensional form, as these are directly relevant to blade design. The parametric comparison of flight conditions and breakdown into harmonics is still carried out in nondimensional form. That is, thrust variation is in terms of C_T/σ , speed in terms of μ , and harmonic content relative to operating rpm (/rev). These nondimensional parameters are direct indicators of proximity to stall, extent of reverse flow, and blade dynamic response. For purposes of plotting, every other azimuthal point is plotted (128 points/rev). Flap bending is positive for upper surface in compression, chord bending is positive for trailing edge in compression, and torsion moment is positive for nose-up. Pitch link load is positive in extension (nose-up).

The rotor frequencies, calculated using UMARC (Ref. 38), and shown in Table 4, are very different for the slowed rotor beyond the third mode. Even though the rotor is stiffer (in /rev, i.e., relative to aerodynamic excitation), the second flap frequency still lies near 3/rev and remains the dominant driver of blade loads. A notable difference at 40% NR is the large frequency gap between the second flap and first torsion modes. The absence of any mode near 4-5/rev has important ramifications on vibratory hub loads, as shown later.

Consider as baseline the condition: $\mu = 0.4$, $C_T/\sigma = 0.071$, and $\alpha_S = 0^\circ$. The effect of rpm variation is studied by sweeping down in rpm, from nominal to 40% NR, at this condition along the points in Table 2. The peak-to-peak blade loads, shown in Fig. 7(a) at selected radial stations, decrease by about 50%. Now with rpm held constant at 40% NR, the variation with advance ratio is studied by considering the sweep up to $\mu = 0.9$ at $\alpha_S = 4^\circ$ (Fig. 7(b)). The thrust level is lower but is the closest obtained to the baseline condition. The peak-to-peak blade loads, shown in Fig. 7(b), build up again, eventually reaching a level similar to the nominal rotor (100% NR, baseline condition) for torsion and levels greater than nominal for flap. Only the chord moment remains lower than nominal (note that the values are revised from Ref. 36).

The flap bending moments are studied in greater detail in Fig. 8. The azimuthal variations of the oscillatory (1/rev and above) flap bending moments are plotted for all radial stations from near the root to the tip (20%-90% R) in three-dimensional plots. The flap bending moments on the nominal rotor (100% NR, baseline condition) are shown in Fig. 8(a). The bending moments at the end of the advance ratio sweep, at $\mu = 0.9$, are shown in Fig. 8(b). Even though the thrust level is lower than the

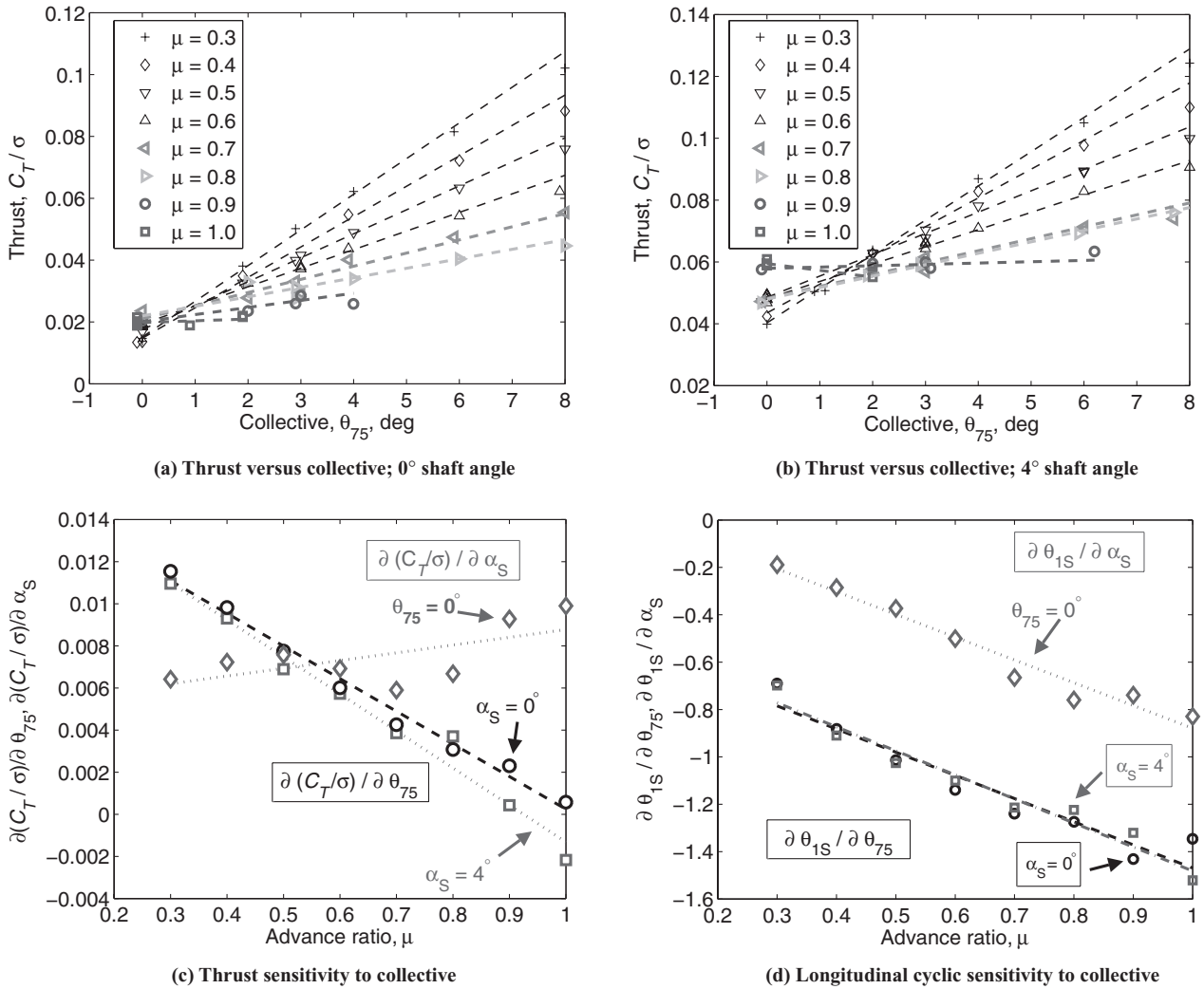


Fig. 4. Thrust and longitudinal cyclic angle variations for advance ratios up to 1.0; 0° and 4° shaft angles; 40% NR.

baseline, the moments are higher. The loading pattern is also qualitatively different. The second mode is still dominant, but the peak loading has now shifted inboard. The bending moments at $\mu = 1.0$, shown in Fig. 8(c), corresponding to a point with an even lower thrust level of $C_T/\sigma = 0.022$ (Point 9175, Table 3), show even greater magnitudes. The advancing side drop is steeper, and the fourth quadrant oscillation is stronger. Note that the dimensional thrusts for both the high-advance-ratio points are very low, 2280 and 784 lb, compared to a thrust of 15,880 lb for the baseline.

The harmonic breakdown of the bending moments is shown in Fig. 9. The left-hand-side plots show the variation with increasing advance ratio at the same thrust level. The right-hand-side plots compare the two highest-advance-ratio cases at high and low thrust levels. The baseline is plotted for comparison. The left-hand-side plots show that the 5/rev harmonic is negligible for the slowed rotor, regardless of advance ratio. The 4/rev harmonic increases dramatically beyond $\mu = 0.7$. The 3/rev harmonic behaves similarly as the baseline and has a comparable magnitude. The 1/rev and 2/rev harmonics, which determine the peak-to-peak variation, are 50–100% higher than baseline inboard of 70% R at the highest advance ratio. The right-hand-side plots indicate that this loading pattern is independent of thrust, remaining the same regardless of $C_T/\sigma = 0.06$ or 0.02. The 3/rev harmonic in fact increases with

a decrease in thrust. Even though these comparisons are not consistent parametric variations (the baseline has a higher thrust and a lower shaft angle, and the $\mu = 1.0$ slowed rotor point has a different shaft angle from the other slowed rotor points), they show that the slowed rotor operating at a negligible dimensional thrust carries bending moments higher than the highest levels of the nominal rotor under high-speed conditions. Net thrust is not even a remote indicator of these loads.

A possible reason behind the high loads is a higher than usual differential airloading between the inboard and outboard sections of the advancing side. If the reverse flow produces little or no lift on the retreating side, this differential airloading is required to trim the rotor. If the reverse flow produces negative lift, then the differential airloading may even be greater, with the outboard stations required to generate negative lift. These conjectures are tested in the next section on pressures and airloads, but the implication here is that the elastic twist on the blades must be significantly high to produce this differential airloading. An examination of the torsion moments indicates that this may indeed be true.

The spanwise distribution of torsion moment harmonics, shown in Fig. 10, indicates a large 1/rev gradient between the inboard and outboard stations (between 30% and 70% R) for the slowed rotor. The phase angle

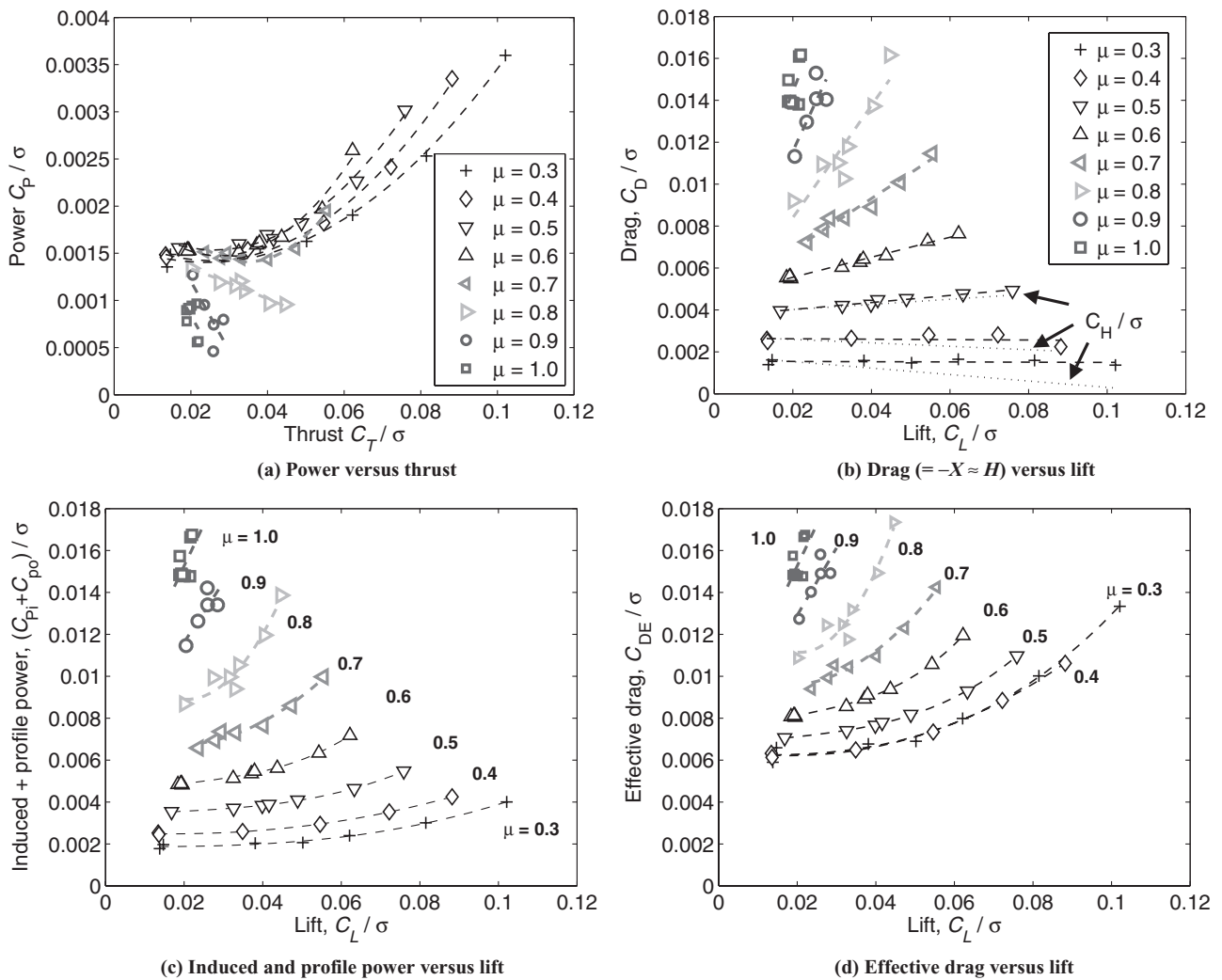


Fig. 5. Power and drag variations for advance ratios up to 1.0; 0° shaft angle; 40% NR.

remains the same. The 2/rev harmonic also shows about a 20% increase at the inboard stations. The vibratory harmonics are significantly lower than the nominal rotor, except for the 3/rev harmonic, which has a comparable magnitude.

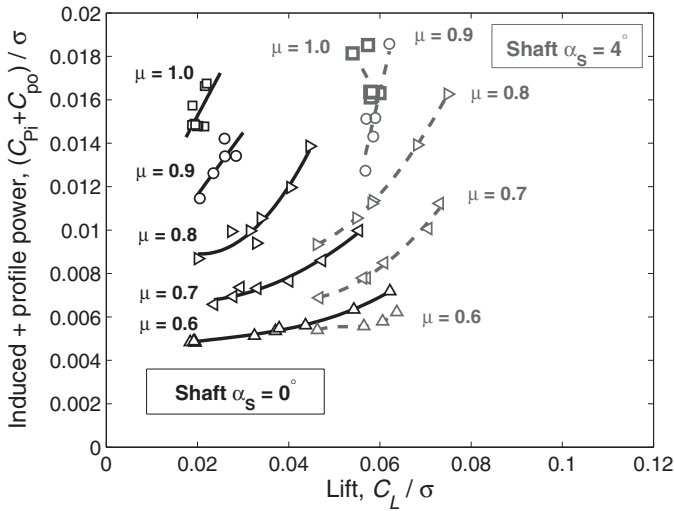
The azimuthal variations of torsion moment at 30% R are compared in Fig. 11(a). In the high-advance-ratio case, the peak loading is more clearly determined by the waveform in the retreating side. The increase in loading around 240° azimuth is a direct consequence of the reverse flow negative lift shifting aft toward 0.75c (0.25c of reverse airfoil) and producing a nose-up pitching moment impulse. Note that the nominal rotor also shows an impulsive behavior in the fourth quadrant—around 300°—but this behavior arises out of a 4/rev response and is phenomenologically different. The increase in torsion loading on the retreating side due to reverse flow was first reported in 1969 by Niebanck (Ref. 31) (on a 9-ft diameter model rotor at $\mu = 1.47$, $\alpha_s = 0^\circ$, and $\theta_{75} = 2^\circ$), and the loading pattern observed here is similar. The retreating side torsion loading is examined in more detail in Fig. 11(b). The figure contains two pairs of plots, one pair each for shaft angles of 0° and 4°. For each shaft angle, collective angles of 0° and 2° are considered, corresponding to the collective sweeps at $\mu = 1.0$ in Table 3. The retreating side impulse increases with collective angle due to an increase in reverse flow angle

of attack and diminishes with shaft angle due to a decrease in reverse flow angle of attack. The reverse flow is clearly less severe for a positive shaft angle.

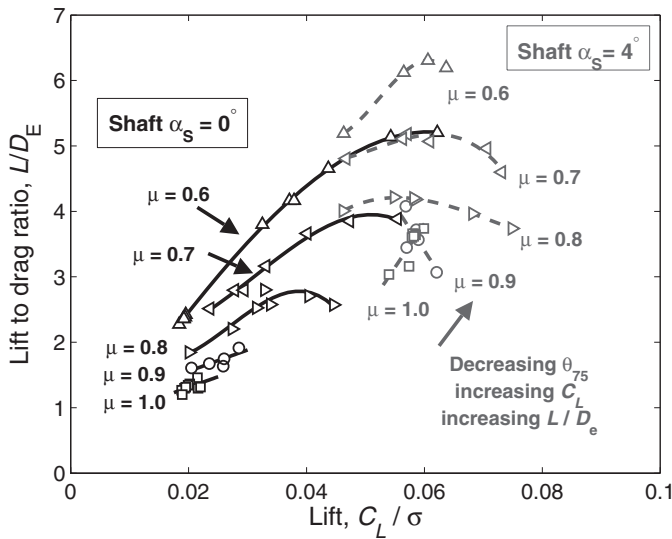
The behavior of the pitch link loads is similar to and consistent with the inboard torsion moment, as expected. Figure 12 summarizes the pitch link load behavior for an advance ratio sweep. A direct consequence of the reverse impulse beyond $\mu = 0.7$ (Fig. 12(a)) appears to be a sudden increase in 3–5/rev harmonic content.

The inboard chord bending moment of the slowed rotor is primarily determined by the damper force, similar to the nominal rotor. With reduction in rpm, the peak-to-peak damper load is reduced. The 1/rev load remains the same, but the 2/rev and higher harmonics decrease. This implies there is little motion at these frequencies to contribute to any substantial loss in damping available at the lag frequency. Thus, lag instability was not a concern during the tests. Increasing advance ratio increases the loads up to nominal levels at $\mu = 1.0$. Further details can be found in Ref. 36.

The effect of advance ratio on vibratory hub loads is evaluated using data from the rotating vertical hub shears and pitch link loads. These measurements can be combined to provide estimates for the vertical force and moments at the hub (but not in-plane forces and torque). Gauge failures



(a) Induced and profile power at two shaft angles



(b) Lift to drag ratios at two shaft angles

Fig. 6. Power and efficiency compared at zero and positive shaft angles; 40% NR.

are compensated for with phase-shifted data from functional gauges. The contributions from hub shear and pitch link loads are both important, particularly when the pitch link loads are high. Ideally, the rotor balance would be used to provide estimates for all the 4/rev vibratory hub loads. However, the transfer function between balance readings and hub loads changes significantly between 4/rev frequency at 100% NR (17.2 Hz)

Table 4. Predicted slowed rotor frequencies compared to nominal

100% NR (/rev)	65% NR (/rev)	40% NR (/rev)	Mode
0.276	0.287	0.318	Lag
1.037	1.040	1.048	Flap
2.83	2.98	3.33	Flap
4.39	5.66	7.33	Torsion
4.69	6.70	10.54	Lag

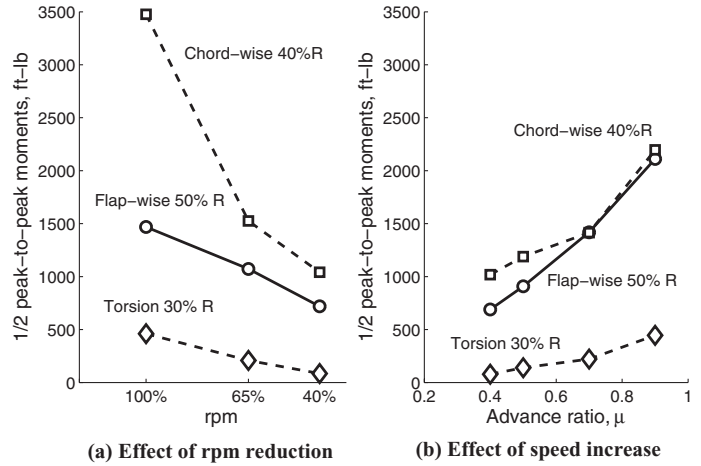


Fig. 7. Effect of rpm reduction and advance ratio increase on 1/2 peak-to-peak blade loads; (a) effect of rpm reduction at $\mu = 0.4$, $C_T/\sigma = 0.07$, $\alpha_s = 0^\circ$; (b) effect of speed increase at 40% NR, $C_T/\sigma = 0.06$, $\alpha_s = 4^\circ$.

and 4/rev frequency at 40% NR (6.9 Hz). A dynamic calibration of the balance that accounts for this change is currently under study.

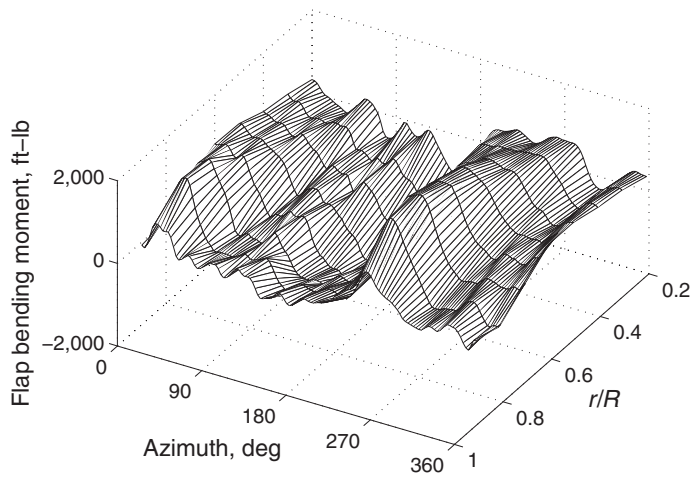
The 4/rev hub loads are shown in Fig. 13 as a function of rpm and tunnel speed. Unlike the blade loads, the hub loads appear to be relatively benign for the slowed rotor. The two nominal points correspond to the $\mu = 0.3$ and 0.4 points in Table 2. These are compared to the slowed rotor points for the two speed sweeps given in the same table—the same conditions for which blade loads were analyzed earlier. The 4/rev vertical force is at least 50% lower for the slowed rotor. Even though the flap bending moments showed a dramatic increase in 4/rev harmonic (Fig. 9), the increase mostly occurred outboard of 40% R and did not affect the shear loading inboard. The hub rolling moment is already low and remains comparable between the nominal and slowed rotors. The hub pitching moment is reduced by more than 50% due to the large reduction of the 5/rev harmonic from the flap bending moments (Fig. 9). The same trend was also observed in the chord bending moments (not shown). The diminished 5/rev is the result of the large frequency gap between the second flap and first torsion modes as shown earlier in Table 4.

In summary, the blade loads on the slowed rotor are comparable to or higher than the nominal rotor beyond an advance ratio of $\mu = 0.8$. Yet, the vibratory hub loads remain benign with at least 50% reduction in vertical force and pitching moments. The blade loads appear to be driven by a high differential airloading between the inboard and outboard sections of the blade potentially caused by a significant elastic twist deformation. The reduction in hub loads is due partly to the frequency gap between second flap and first torsion modes leading to diminished 5/rev blade loads. At advance ratios beyond 0.9, the peak torsion loads were determined primarily by a nose-up impulsive loading on the retreating side.

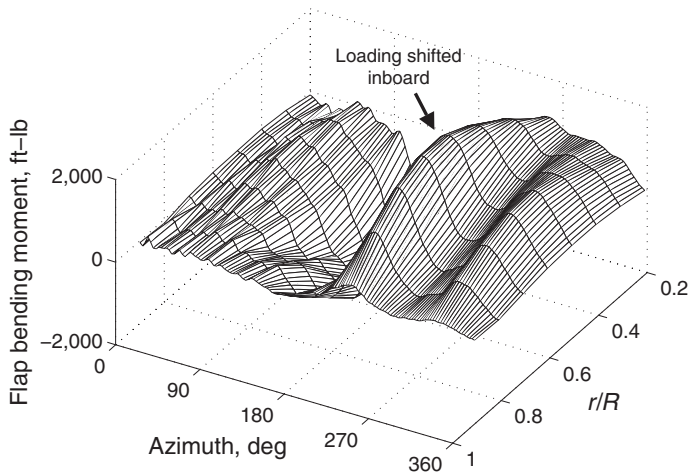
Blade Pressures and Airloads

This section analyzes the blade surface pressures and sectional airloads to uncover phenomena that are unique to the slowed rotor.

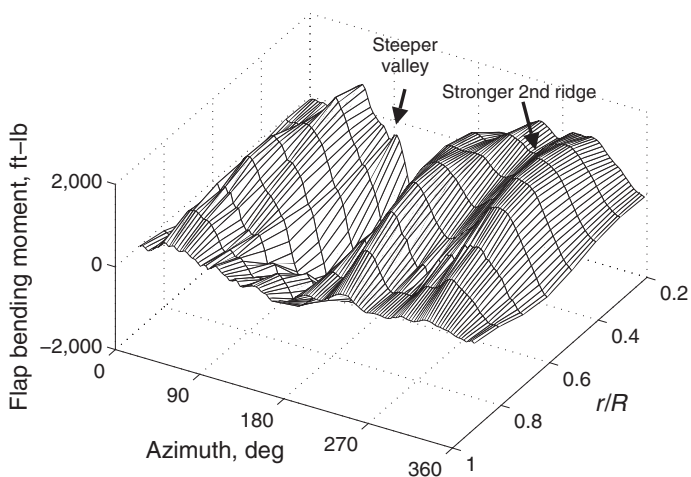
The radial stations where enough pressure transducers remained functional for sectional airloads calculation were 22.5%, 86.5%, 92%, and 99% R. Most of the inboard sections that are important for reverse flow, 40%–77.5% R, all suffered loss of transducers. Nevertheless, many of the transducers remained functional in these stations and a study of these transducers provides significant insights into the flow characteristics in



(a) 100% NR; $\mu = 0.4, C_T/\sigma = 0.071 (T = 15,880 \text{ lb}), \alpha_s = 0^\circ$



(b) 40% NR; $\mu = 0.9, C_T/\sigma = 0.063 (T = 2280 \text{ lb}), \alpha_s = 4^\circ$



(c) 40% NR; $\mu = 1.0, C_T/\sigma = 0.022 (T = 784 \text{ lb}), \alpha_s = 0^\circ$

Fig. 8. Flap bending moments (mean removed); nominal versus slowed rotor, at high and low thrust levels.

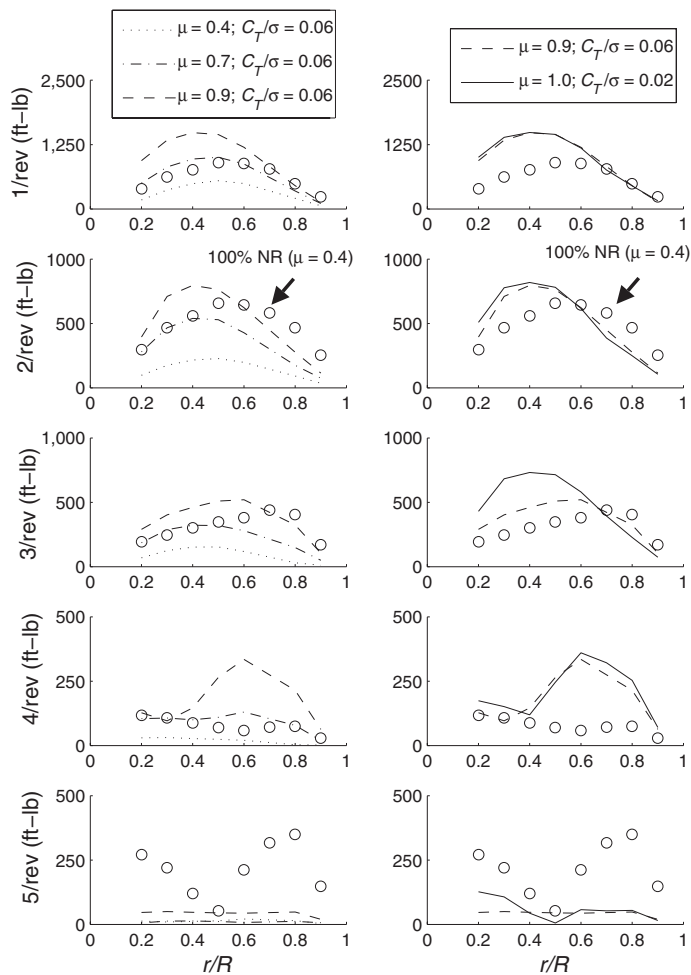


Fig. 9. Flap bending moment harmonics for nominal and 40% NR slowed rotor; nominal: $\mu = 0.4, C_T/\sigma = 0.071, \alpha_s = 0^\circ$ (shown as symbols (o)); slowed: $\mu = 0.4-0.9, C_T/\sigma = 0.063, \alpha_s = 4^\circ$ and $\mu = 1.0, C_T/\sigma = 0.022, \alpha_s = 0^\circ$ (shown as lines).

this regime. These phenomena can then be associated with the structural load patterns observed in the preceding sections. Note that the pressure plots presented in this section are revised from those originally published in Ref. 36.

The azimuthal variation of pressures is studied as offset plots of $-M^2 C_p$, where M is the sectional Mach number and C_p the pressure coefficient. In these plots, only the leading-edge (or nearest working transducer) values are measured, the rest are offset in steady values to reveal chordwise and azimuthal trends. Because negative pressure is plotted, an increase implies flow acceleration, hence suction. For accelerated flow, the onset of surface supersonic flow is estimated by the one-dimensional steady isentropic relation:

$$C_p = \frac{2}{\gamma M^2} \left[\left\{ \left(1 + \frac{\gamma - 1}{2} M_l^2 \right) / \left(1 + \frac{\gamma - 1}{2} M^2 \right) \right\}^{\frac{\gamma}{1-\gamma}} - 1 \right] \quad (3)$$

where M_l is the local surface Mach number. Substituting $M_l = 1$ and M at any azimuth provides an estimate $C_p = C_p^*$ of the surface pressure for onset of supersonic flow.

Consider one of the most severe reverse flow points (highest advance ratio, highest collective, zero shaft angle): $\mu = 1.0, \theta_{75} = 2^\circ$, and $\alpha_s = 0^\circ$ (Point 9175). The upper and lower surface pressures at 22.5% R

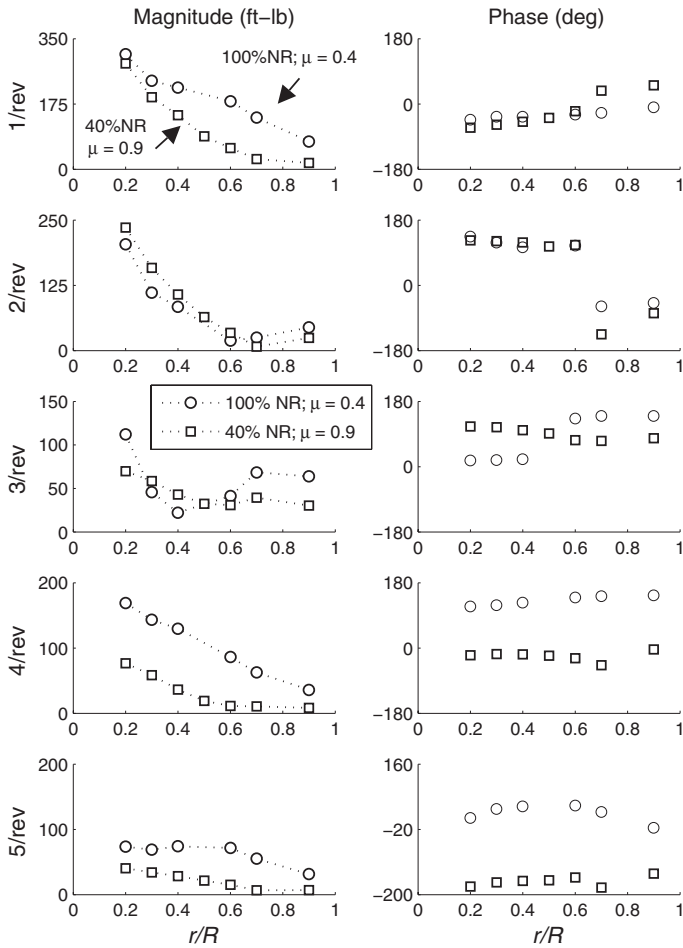
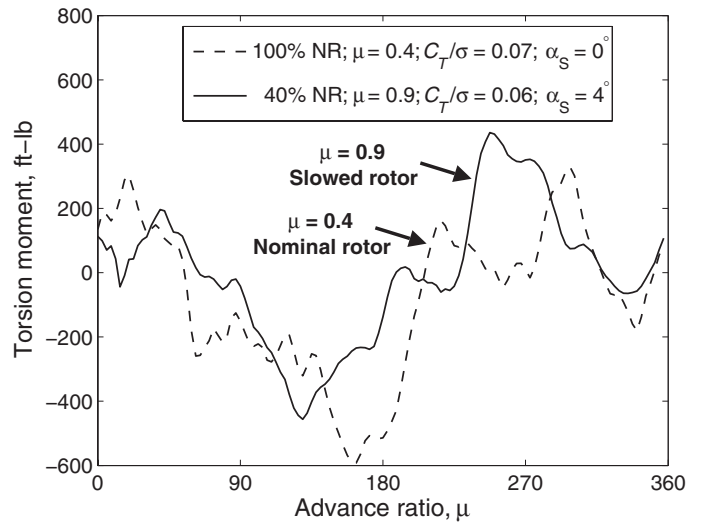


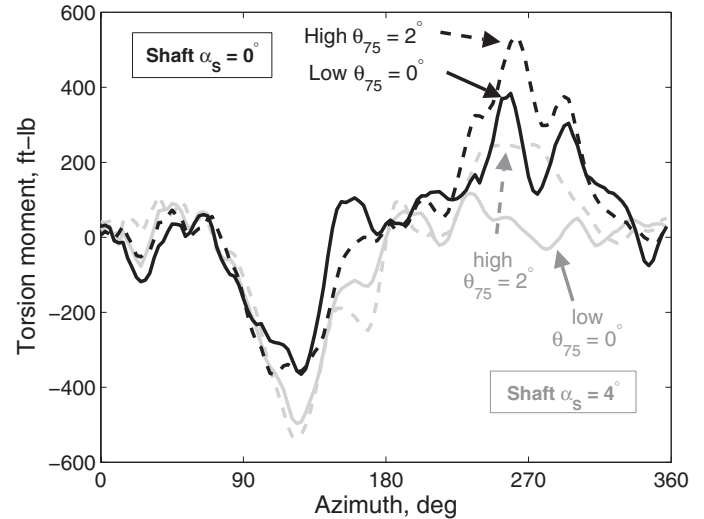
Fig. 10. Torsion moment harmonics for nominal and 40% NR slowed rotor; nominal: $\mu = 0.4$, $C_T/\sigma = 0.07$, $\alpha_S = 0^\circ$; slowed: $\mu = 0.9$, $C_T/\sigma = 0.06$, $\alpha_S = 4^\circ$.

are shown in Figs. 14(a) and 14(b), respectively. The azimuthal extent of reverse flow is demarcated in the plots by vertical lines. There is suction on both surfaces in the reverse flow region, but on the lower surface the suction appears to increase in strength from leading-edge (LE) toward trailing-edge (TE). If the TE were to behave as the effective LE of the reversed airfoil, greater suction is expected at the TE.

Next, consider the test point: $\mu = 0.8$, $\theta_{75} = 8^\circ$, and $\alpha_S = 0^\circ$ (Point 9159). In addition to the transducers at 22% R , the lower surface transducers at a slightly outboard station (40% R) are all functional. First, consider the upper and lower surface pressures at 22.5% R (Figs. 15(a) and 15(b), respectively). The advance ratio is lower in this flight, but because the collective angle is significantly higher, significant reverse flow effects are expected. The figures show that there is suction on both surfaces as before, but suction on the lower surface appears more marked. Compared to the previous point, the lower surface impulses are sharper and have a greater azimuthal movement. The impulse at $0.107c$ occurs at a slightly delayed azimuth compared to that at $0.203c$, the impulse at $0.203c$ occurs at a slightly delayed azimuth compared to that at $0.395c$, and so on. This is a signature of a stall vortex—a reverse chord stall vortex—triggered at the TE and sweeping across the lower surface in reverse chord direction toward the LE. The reason for the double peak is not clear, but since the TE is sharp it is possible that two vortices are formed one after the other eventually merging near the LE. But the leading-edge, unlike the trailing-edge, is not sharp and the vortex



(a) Torsion moment at 30% R for nominal and 40% NR slowed rotor; nominal: $\mu = 0.4$, $C_T/\sigma = 0.07$, $\alpha_S = 0^\circ$; slowed: $\mu = 0.9$, $C_T/\sigma = 0.06$, $\alpha_S = 4^\circ$



(b) Study of retreating side impulse in torsion moment (30% R) at $\mu = 1.0$ for a 40% NR slowed rotor showing increased severity at lower shaft angle and higher collective

Fig. 11. Torsion moments at 30% R compared between nominal and slowed rotors.

may turn around to the upper surface. The pressure pulses on the upper surface (Fig. 15(a)), over a short expanse of 20% span near the nose and moving rearward, may indicate such a phenomenon. The azimuthal movement is small because the span location is very far inboard. The lower surface pressures at 40% R , a station further outboard, provide a clearer illustration of the reverse chord dynamic stall phenomenon. Here, as seen from Fig. 16, the stall vortex pulse displays a wider azimuthal movement—forming around $0.819c$ at 250° and leaving the LE at 275° . The stall vortex pulses are responsible for the retreating side impulse in sectional pitching moments shown later in Fig. 18 and the torsion loads shown earlier in Fig. 11(b).

To examine stations further outboard, consider the highest-advance-ratio point again: $\mu = 1.0$, $\theta_{75} = 2^\circ$, and $\alpha_S = 0^\circ$ (Point 9175). The pressures at 77.5% R are shown in Figs. 17(a) and 17(b). The reverse flow region appears tranquil—with no unsteady airloading—indicating

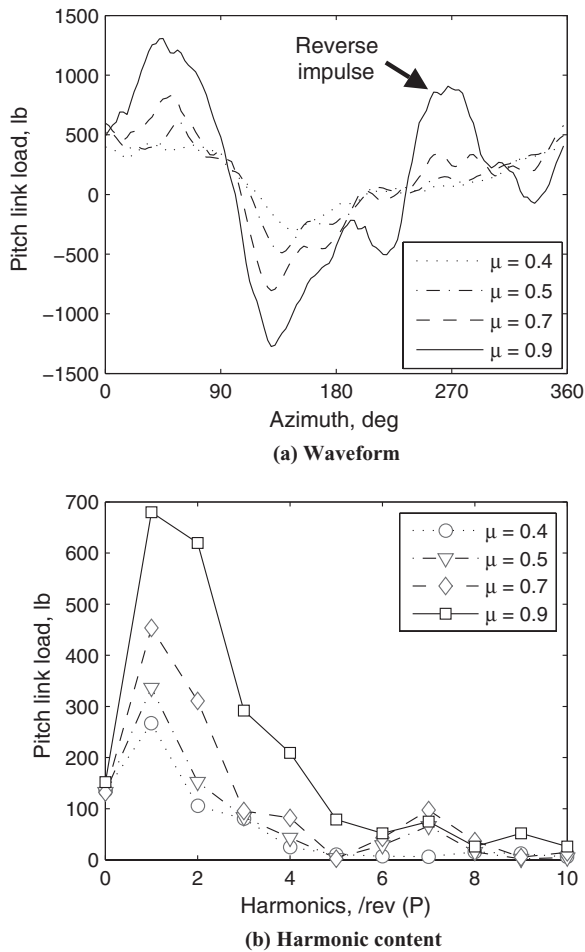


Fig. 12. Pitch link load variation with advance ratio; $\mu = 0.4\text{--}0.9$, $C_T/\sigma \approx 0.06$, $\alpha_S = 4^\circ$; 40% NR.

the possibility of a completely separated flow. On the advancing side, high suction indicates significant flow accelerations accompanied by the onset of local supersonic flow. The estimated azimuthal extent of the supersonic flow is demarcated in Fig. 17(b) by the intersection of the sonic line (Eq. (3)) with $M_l = 1.0$) with the pressure lines. Only the LE (within 1% chord) experiences supersonic flow at this station, hence this is not a shock. A similar pattern is seen further outboard at 92% R , but none at 86.5% R contrary to what was reported in Ref. 36. Note that the advancing tip Mach number M_A is only 0.52, the thrust C_T/σ a mere 0.022, and the longitudinal cyclic only -2.7° . Local supersonic flow under such conditions appears to support the conjecture that the blades are carrying a significant amount of elastic twist. This is further supported by the high negative loading seen in the sectional airloads at this station.

Figure 18 shows the inboard (22.5% R) and outboard (86.5% R) sectional airloads for the two high-advance-ratio conditions. The inboard station (22.5% R) shows the reverse chord dynamic stall vortex impulse on the retreating side. The normal force increment ($\Delta M^2 c_n$) of about 0.05 and the associated nose-up pitching moment increment ($\Delta M^2 c_m$) of about 0.0125 indicate that the reverse flow lift now acts nominally at a 0.25c offset from the local 0.25c from the LE, i.e., effectively at 0.5c, not 0.75c. The reverse chord stall vortex, unlike a conventional stall vortex, moves toward 0.25c and not away from it and is therefore responsible for this shorter shift. For the same reason, the reverse chord stall vortex is less detrimental to pitching moments (and torsion loads). Its contribution

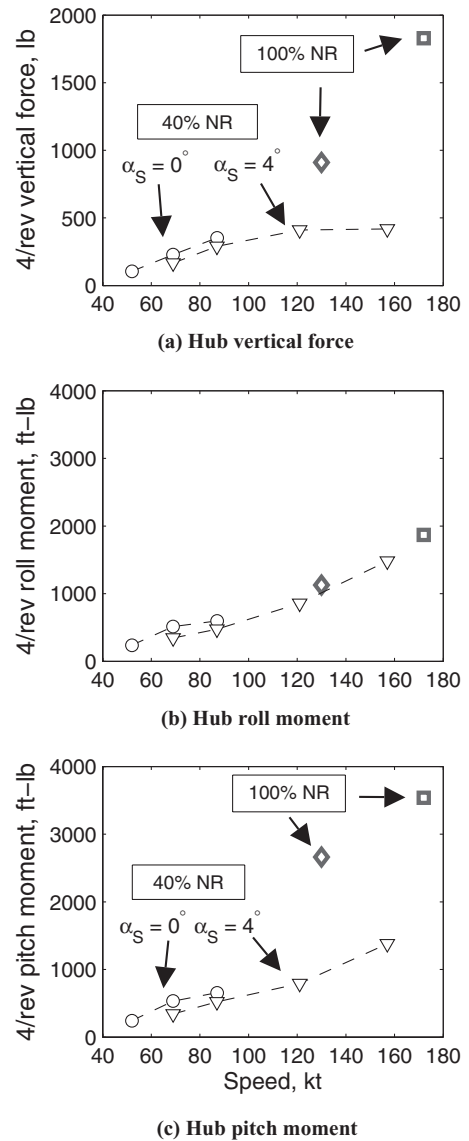
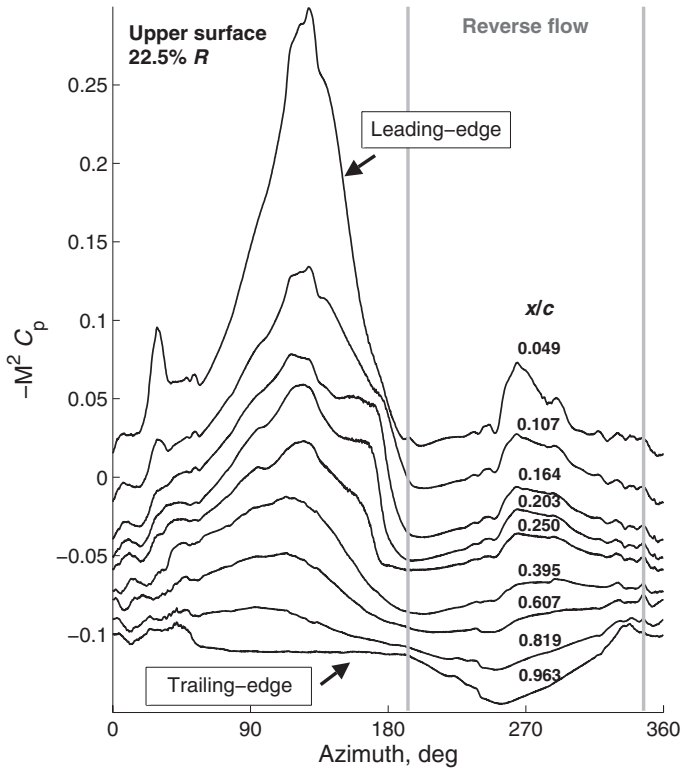


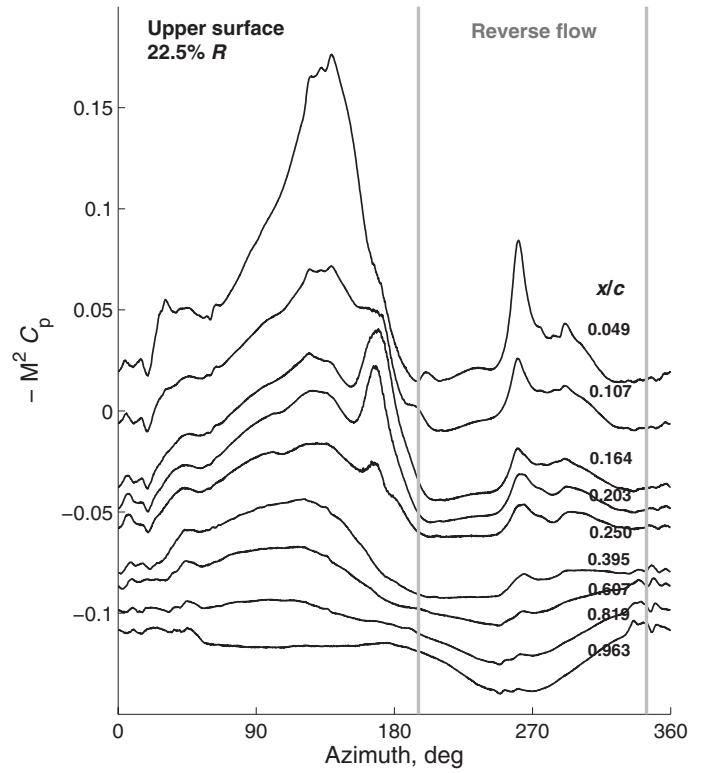
Fig. 13. Vibratory hub loads versus speed for nominal and 40% NR slowed rotors; nominal: $\mu = 0.3$, $C_T/\sigma = 0.082$, $\alpha_S = 0^\circ$ (Point 6619, \diamond); $\mu = 0.4$, $C_T/\sigma = 0.071$, $\alpha_S = 0^\circ$, (Point 6912, \square); slowed: speed sweep at $C_T/\sigma = 0.06$, $\alpha_S = 0^\circ$ (\circ) and at $C_T/\sigma = 0.06$, $\alpha_S = 4^\circ$ (∇).

to chord force is also substantial—the amplitude of the spike is greater than the peak amplitude of chord force variation at the outboard station (86.5% R). The outboard station (86.5% R) is immersed deeply into negative lift. At $\mu = 1.0$, almost the entire advancing side at this station carries a negative loading. The negative lift is also indicative of a high differential airloading that must exist on the advancing side.

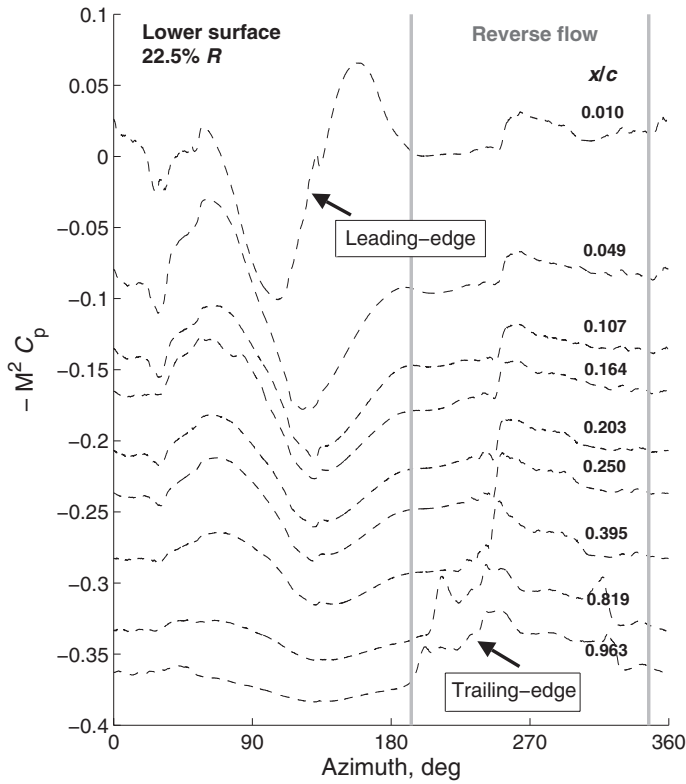
In summary, the retreating side lower surface shows evidence of reverse chord dynamic stall phenomenon at the inboard stations (40% R and inboard). The advancing side lower surface shows evidence of local transonic flow at the outboard stations (77.5% R and outboard). The reverse chord dynamic stall inboard is a key contributor to the nature of retreating side impulse in torsion loading. The shift in lift is not a simple aft movement of 0.5c but depends on this stall phenomenon. The reverse chord stall inboard on the retreating side together with transonic flow outboard on the advancing side contribute to significant elastic



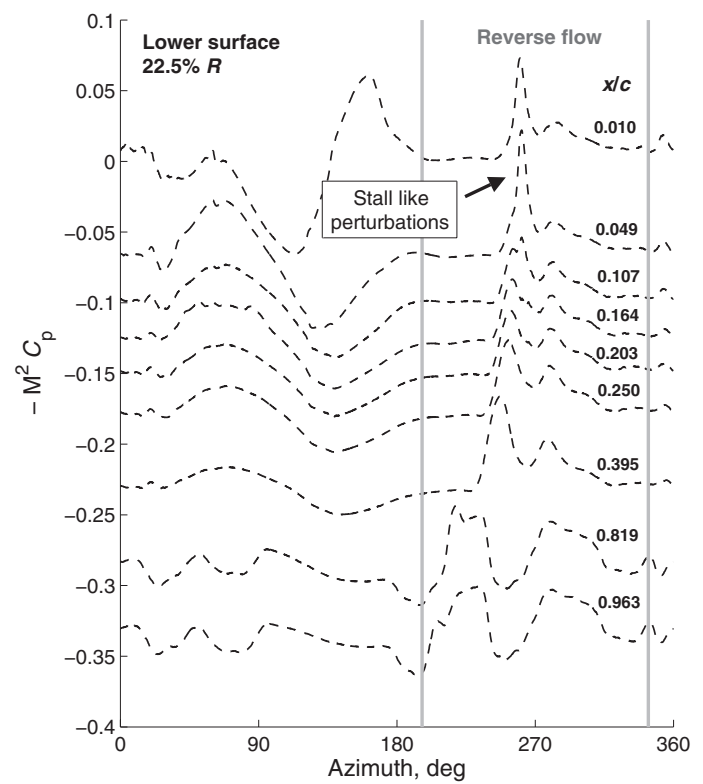
(a) Upper surface pressures



(a) Upper surface pressures



(b) Lower surface pressures



(b) Lower surface pressures

Fig. 14. Surface pressures at 22.5% R ; $\mu = 1.0$; $C_T/\sigma = 0.022$ ($\theta_{75} = 2^\circ$), $\alpha_S = 0^\circ$; 40% NR (Point 9175).

Fig. 15. Surface pressures at 22.5% R ; $\mu = 0.8$; $C_T/\sigma = 0.045$ ($\theta_{75} = 8^\circ$), $\alpha_S = 0^\circ$; 40% NR (Point 9159).

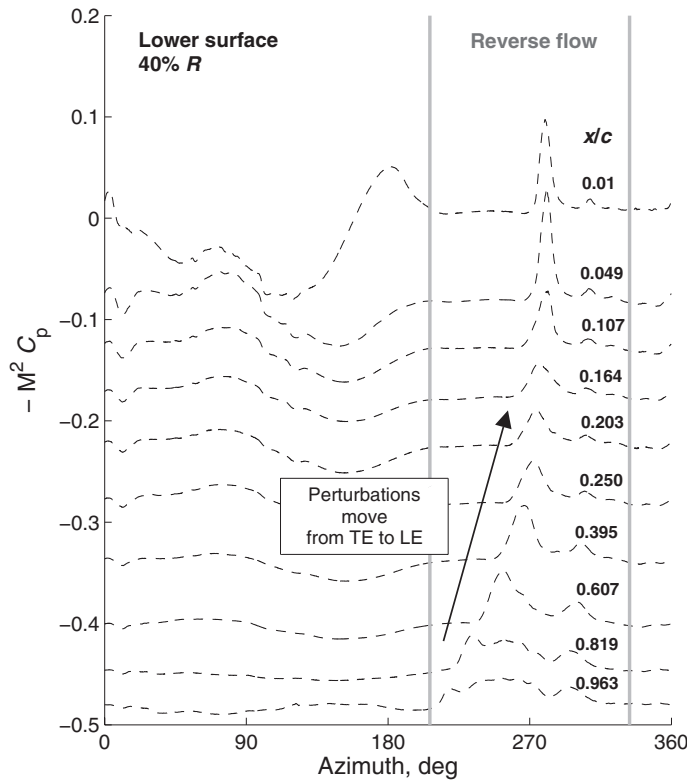


Fig. 16. Lower surface pressures at 40% R; $\mu = 0.8$; $C_T/\sigma = 0.045$ ($\theta_{75} = 8^\circ$), $\alpha_S = 0^\circ$; 40% NR (Point 9159).

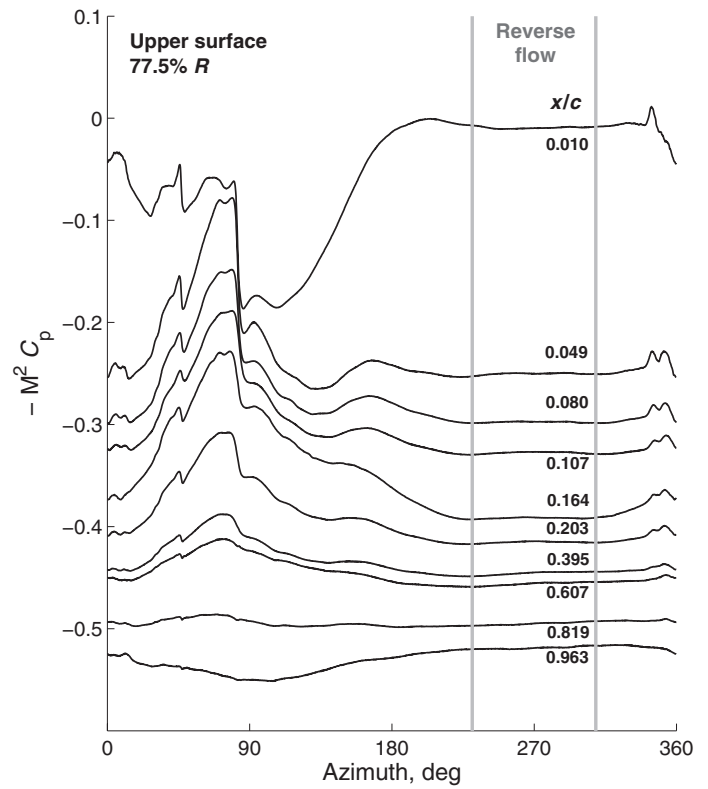
twist deformations. The resulting high differential airloading immerses an outboard station (86.5% R) in negative lift over a large region in the advancing side.

Summary and Conclusions

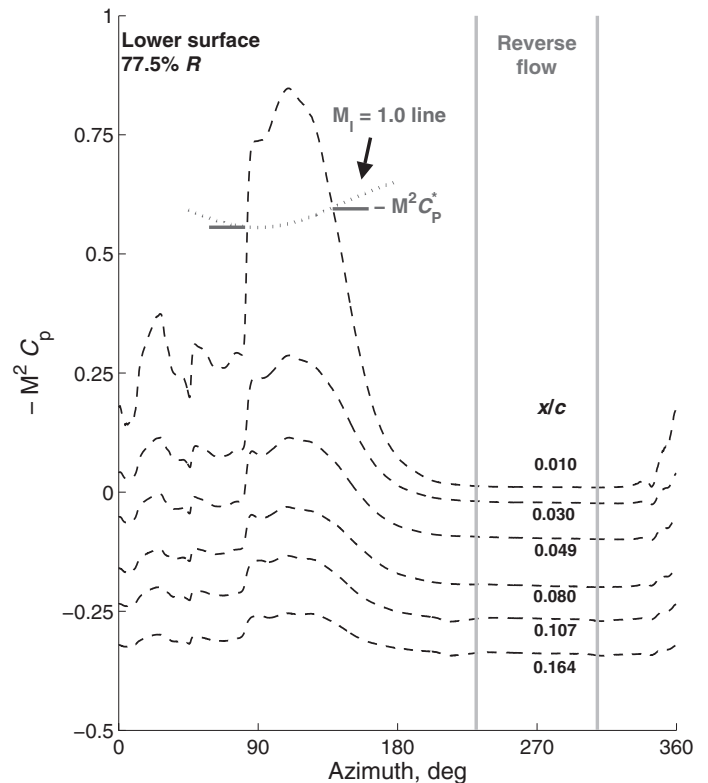
A full-scale UH-60A rotor was tested in the NFAC 40- by 80-ft wind tunnel under slowed rpm conditions (65% and 40% of nominal) reaching a maximum advance ratio of 1.0. Comprehensive measurements of performance, blade loads, hub loads, and pressures/airloads were acquired. An examination of the measurements was presented with emphasis on the fundamental understanding of the aeromechanical phenomena unique to this regime. The intent of the test was to gain useful knowledge for the design of high-speed, high-efficiency, slowed rotors of the future and acquire a challenging database for validation of advanced analyses. Based on this research, the following conclusions are drawn:

1) The dynamic loads on the slowed rotor, operating at advance ratios $\mu = 0.8$ and beyond, are comparable to or significantly greater than those encountered by the nominal rotor at $\mu = 0.3-0.4$. The primary reason appears to be a high differential airloading between the inboard and outboard sections of the advancing side. This is how the rotor trims in the presence of large regions of reverse flow (negative or zero lift) on the retreating side. The net thrust level is not even a remote indicator of these load levels.

2) The requirement to achieve trim with increasing reverse flow on the retreating side results in an increasing longitudinal cyclic requirement which together with the high built-in twist on this rotor drive the advancing side outboard stations to negative lift. For example, at $\mu = 1.0$ and $C_T/\sigma = 0.022$, the 86.5% R station is found negatively loaded almost over the entire first and second quadrants. The negative loading is



(a) Upper surface pressures



(b) Lower surface pressures

Fig. 17. Surface pressures at 77.5% R; $\mu = 1.0$; $C_T/\sigma = 0.022$ ($\theta_{75} = 2^\circ$), $\alpha_S = 0^\circ$; 40% NR (Point 9175).

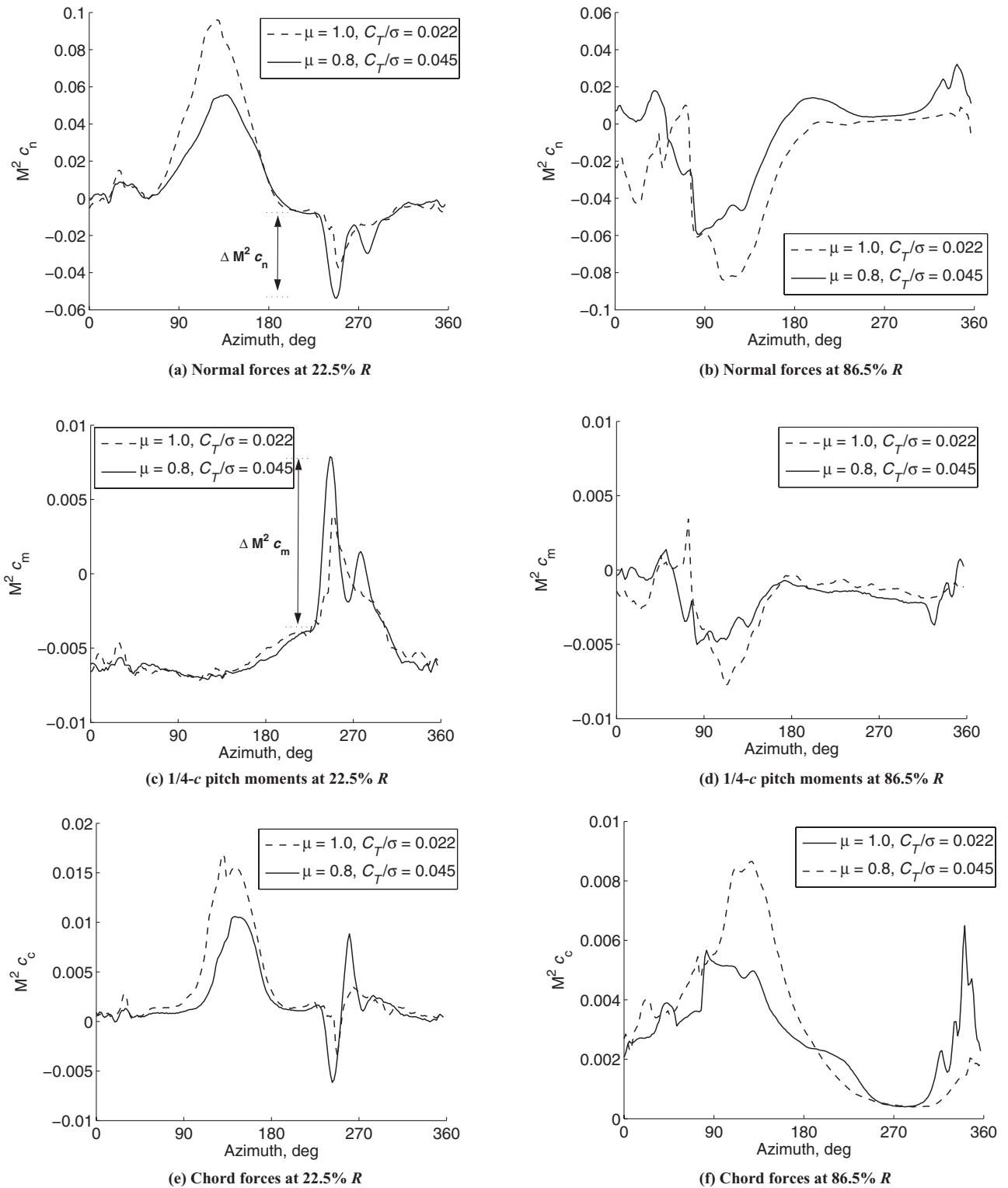


Fig. 18. Sectional airloads at 22.5% and 86.5% R for the 40% NR slowed rotor at two high-advance-ratio points: $\mu = 1.0, C_T/\sigma = 0.022, \theta = 2^\circ, \alpha_S = 0^\circ$ (Point 9175); and $\mu = 0.8, C_T/\sigma = 0.045, \theta = 8^\circ, \alpha_S = 0^\circ$ (Point 9159).

aggravated by an unusually high 1/rev elastic twist differential across the span.

3) The principal source of the high elastic twist differential appear to be a nose-up reverse flow impulse in pitching moments. A secondary mechanism can be the onset of transonic flow on the lower surface of the advancing side occurring as far inboard as 77.5% R.

4) The positively loaded (suction) lower surface of the reverse flow region on the retreating side shows evidence of reverse chord dynamic stall—a phenomenon unique to the high-advance-ratio regime. Here, the dynamic stall vortices sweep across the chord in the reverse direction—from the trailing-edge to the leading-edge—leave signatures on both surfaces, and contribute to less detrimental torsion loads than

conventional stall. Other than this phenomenon, the reverse flow region appears tranquil and does not contribute to any significant unsteady air-loading.

5) At advance ratios $\mu = 0.8$ and beyond, the peak torsion loads are significantly affected by the nose-up reverse flow impulse on the retreating side. The impulse results from the downward lift and an aft center of pressure movement, but the amount of this shift and the resulting waveform is determined by the onset of reverse chord dynamic stall.

6) Even though the blade loads are high for the slowed rotor operating at high advance ratios, the vibratory hub loads (dominantly 4/rev for this rotor) are benign. The 4/rev vertical force is reduced by at least 50% compared to the nominal rotor. The 4/rev pitching moment is reduced by at least 50%–75% due to a reduction of 5/rev blade bending moments. This reduction is in turn caused by the wide rotor frequency gap between the second flap (3.33/rev) and first torsion (7.33/rev) modes at 40% NR.

7) The performance measurements at high advance ratios were consistent with previous test data. The thrust reversal with collective angle around $\mu = 0.9 - 1.0$ was observed as expected. The rotor is more efficient at a positive shaft angle but at the expense of greater drag.

Acknowledgments

The slowed rotor test was a collaborative endeavor between NASA, U.S. Army, and the U.S. Air Force's NFAC team. We acknowledge Sikorsky Aircraft's review and recommendations of the special motions and loads allowables for the test. We thank Wayne Johnson and Frank Harris for their advice during test planning and preparation.

References

- ¹Rosen, K. M., "A Prospective: The Importance of Propulsion Technology to the Development of Helicopter Systems with a Vision for the Future, The 27th Alexander A. Nikolsky Lecture," *Journal of the American Helicopter Society*, Vol. 53, (4), October 2008, pp. 307–337.
- ²Stevens, M. A., Handschuh, R. F., and Lewicki, D. G., "Concepts for Variable/Multi-Speed Rotorcraft Drive System," NASA TM-2008-215276, September 2008.
- ³Snyder, C. A., Robuck, M., Wilkerson, J., and Nordstrom, C., "Summary of the Large Civil Tiltrotor (LCTR2) Engine Gearbox Study," International Powered Lift Conference, Philadelphia, PA, October 5–7, 2010.
- ⁴Blackwell, R., and Millott, T., "Dynamic Design Characteristics of the Sikorsky X2 TD Aircraft," American Helicopter Society 64th Annual Forum Proceedings, Montreal, Canada, April 29–May 1, 2008.
- ⁵Bagai, A., "Aerodynamic Design of the X2 TD Main Rotor," American Helicopter Society 64th Annual Forum Proceedings, Montreal, Canada, April 29–May 1, 2008.
- ⁶Karem, A. E., "Optimum Speed Rotor," U.S. Patent No. 6007298, December 28, 1999.
- ⁷Waide, W. M., and Karem, A. E., "Rotorcraft Engine and Rotor Speed Synchronization," U.S. Patent No. 7866598, January 11, 2011.
- ⁸Charnov, B. H., *From Autogiro to Gyroplane: The Amazing Survival of an Aviation Technology*, Praeger Publishers, Westport, CT, 2003.
- ⁹Marks, M. D., "Flight Test Development of XV-1 Convertiplane," American Helicopter Society 3rd Annual National Forum Proceedings, Dallas, TX, October 8, 1956.
- ¹⁰Gibbings, D., "The Fairey Rotodyne—Technology Before Its Time?," 2003 Cierva Lecture, *The Aeronautical Journal*, Vol. 108, (1089), November 2004, pp. 565–574.
- ¹¹Robb, R. L., "Hybrid Helicopters: Compounding the Quest for Speed," *Vertiflight*, Vol. 2, Summer 2006, pp. 30–54.
- ¹²Spreuer, W. E., "Experimental Flight Tests of the XH-51A Compound Helicopter," *Journal of the American Helicopter Society*, Vol. 13, (3), July 1969, pp. 64–69.
- ¹³Johnson, W., Yamauchi, G. K., and Watts, M. E., "NASA Heavy Lift Rotorcraft Systems Investigation," NASA TP 2005-213467, December 2005.
- ¹⁴Yeo, H., and Johnson, W., "Aeromechanics Analysis of a Heavy Lift Slowed-Rotor Compound Helicopter," *Journal of Aircraft*, Vol. 44, (2), March–April 2009, pp. 501–508.
- ¹⁵Floros, M. W., and Johnson, W., "Stability and Control Analysis of the Slowed-Rotor Compound Helicopter," *Journal of the American Helicopter Society*, Vol. 52, (3), July 2007, pp. 239–253.
- ¹⁶Yeo, H., and Johnson, W., "Optimum Design of a Compound Helicopter," *Journal of Aircraft*, Vol. 46, (4), July–August 2009, pp. 1210–1221.
- ¹⁷Floros, M. W., and Johnson, W., "Performance Analysis of the Slowed-Rotor Compound Helicopter Configuration," *Journal of the American Helicopter Society*, 54, 022002 (2009).
- ¹⁸Ormiston, R. A. "Applications of the Induced Power Model and Performance of Conventional and Advanced Rotorcraft," American Helicopter Society Aeromechanics Specialists' Conference, San Francisco, CA, January 20–22, 2010.
- ¹⁹Walsh, D., Weiner, S., Arifian, K., Bagai, A., Lawrence, T., and Blackwell, R., "Development Testing of the Sikorsky X2 Technology™ Demonstrator," American Helicopter Society 65th Annual Forum Proceedings, Grapevine, TX, May 27–29, 2009.
- ²⁰Roesch, P., "Fast Hybrid Helicopter with Long Range with Longitudinal Trim Control," U.S. Patent No. 2010/0224720 A1, September 9, 2010.
- ²¹Eglin, P., "Drive Control and Regulation Method and System for a Hybrid Helicopter," U.S. Patent No. 2010/0310371 A1, December 9, 2010.
- ²²Geiger, B., Piasecki, F. W., Horn, J. F., Lotterio, M., and Schifferle, P., "Challenges of Flight Control in a Compound Helicopter," AHS, AIAA, SAE, RAeS International Powered Lift Conference, October 5–7, 2010.
- ²³Carter, J., "CarterCopter—A High Technology Gyroplane," American Helicopter Society Vertical Lift Design Conference, San Francisco, CA, January 19–21, 2000.
- ²⁴Wheatley, J. B., and Hood, M. J., "Full-Scale Wind-Tunnel Tests of a PCA-2 Autogiro Rotor," NACA Report No. 515, 1935.
- ²⁵Sweet, G. E., Jenkins, J. L., Jr., and Winston, M. M. "Wind-Tunnel Measurements on a Lifting Rotor at High Thrust Coefficients and High Tip-Speed Ratios," NASA TN D-2462, September 1964.
- ²⁶Jenkins, J.L., Jr., "Wind Tunnel Investigation of a Lifting Rotor at Tip-Speed Ratios from 0.65 to 1.45," NASA TN D-2628, February 1965.
- ²⁷McCloud, J. L., III, and Biggers, J. C., "An Investigation of Full-Scale Helicopter Rotors At High Advance Ratios and Advancing Tip Mach Numbers," NASA TN D-4632, July 1968.
- ²⁸Charles, B. D., and Tanner, W. H., "Wind Tunnel Investigation of Semirigid Full-Scale Rotors Operating at High Advance Ratios," USAAVLABS Technical Report 69-2, January 1969.
- ²⁹Harris, F. D., "Rotor Performance at High Advance Ratio; Theory versus Test," NASA CR 2008-215370, October 2008.
- ³⁰Meyer, J. R., and Falabella, G., Jr., "An Investigation of the Experimental Aerodynamic Loading on a Model Helicopter Rotor Blade," NACA TN 2953, May 1953.
- ³¹Niebanck, C. F., "A Comparison of Dynamically Scaled Model Rotor Test Data with Discrete Azimuth Aeroelastic Stability Theory," American Helicopter Society 25th Annual National Forum Proceedings, Washington, DC, May 14–16, 1969; see also discussion of the paper in the same

conference: Ham, N. D., and Johnson, W., "A Comparison of Dynamically Scaled Model Rotor Test Data with Discrete Azimuth Aeroelastic Stability Theory."

³²Ewans, J. R., and Krauss, T. A., "Model Wind Tunnel Tests of a Reverse Velocity Rotor System," Prepared for Naval Air Systems Command Under Contract No. N00019-71-C-0506 by Fairchild Republic Division, Farmingdale, NY, January 1973.

³³Quackenbush, T. R., Wachspress, D. A., McKillip, R. M., and Sibia, M. J., "Aerodynamic Studies of High Advance Ratio Rotor Systems," American Helicopter Society 67th Annual Forum Proceedings, Virginia Beach, VA, May 3–5, 2011.

³⁴Berry, B., and Chopra, I., "Wind Tunnel Testing for Performance and Vibratory Loads of a Variable-Speed Mach-Scale Rotor," American Helicopter Society 67th Annual Forum Proceedings, Virginia Beach, VA, May 3–5, 2011.

³⁵Norman, T. R., Shinoda, P., Peterson, R. L., and Datta, A., "Full-Scale Wind Tunnel Test of The UH-60A Airloads Rotor," American Helicopter Society 67th Annual Forum Proceedings, Virginia Beach, VA, May 3–5, 2011.

³⁶Datta, A., Yeo, H., and Norman, T. R., "Experimental Investigation and Fundamental Understanding of a Slowed UH-60A Rotor at High Advance Ratios," American Helicopter Society 67th Annual Forum Proceedings, Virginia Beach, VA, May 3–5, 2011.

³⁷Kufeld, R. M., Balough, D. L., Cross, J. L., Studebaker, K. F., Jennison, C. D., and Bousman, W. G., "Flight Testing of the UH-60A Airloads Aircraft," American Helicopter Society 50th Annual Forum Proceedings, Washington DC, May 11–13, 1994.

³⁸Datta, A., and Chopra, I., "Validation of Structural and Aerodynamic Modeling Using UH-60A Airloads Program Data," *Journal of the American Helicopter Society*, Vol. 51, (1), January 2006, pp. 43–58.